Acta Biomaterialia 198 (2025) 302–318

Contents lists available at ScienceDirect

Acta Biomaterialia

journal homepage: www.elsevier.com/locate/actbio

Full length article

Human bone ultrastructure in 3D: Multimodal correlative study combining nanoscale X-ray computed tomography and quantitative polarized Raman spectroscopy

Tatiana Kochetkova [a,b,1,*], Tatiana Kormilina [c,d,1,**], Silvan Englisch [c], Dominik Drobek [c], Benjamin Apeleo Zubiri [c], Oliver Braun [e,f], Michel Calame [e,f,g], Stefan Remund [h], Beat Neuenschwander [h], Johann Michler [a], Philippe Zysset [b], Erdmann Spiecker [c,***], Jakob Schwiedrzik [a,i,****]

[a] Empa, Swiss Federal Laboratories for Materials Science and Technology, Laboratory for Mechanics of Materials & Nanostructures, Feuerwerkerstrasse 39, CH-3602 Thun, Switzerland
[b] ARTORG Center for Biomedical Engineering Research, University of Bern, Switzerland
[c] Institute of Micro- and Nanostructure Research (IMN) and Center for Nanoanalysis and Electron Microscopy (CENEM), IZNF, Friedrich-Alexander-Universität Erlangen-Nürnberg, Germany
[d] Graz Center for Electron Microscopy (ZFE) and Institute of Electron Microscopy and Nanoanalysis (FELMI), Graz University of Technology, Austria
[e] Empa, Swiss Federal Laboratories for Materials Science and Technology, Transport at Nanoscale Interfaces Laboratory, Dübendorf, Switzerland
[f] Department of Physics, University of Basel, Switzerland
[g] Swiss Nanoscience Institute, University of Basel, Switzerland
[h] Institute for Applied Laser, Photonics and Surface technologies (ALPS), Bern University of Applied Sciences, Burgdorf, Switzerland
[i] Empa, Swiss Federal Laboratories for Materials Science and Technology, Laboratory for High Performance Ceramics, Dübendorf, Switzerland

ARTICLE INFO

Keywords:
Lamellar bone ultrastructure
Lacuno-canalicular network
Mineralized collagen fibrils orientation
Lamellar organization
Multimodal characterization

ABSTRACT

Unique mechanical properties of cortical bone are defined by the arrangement and ratio of its organic and inorganic constituents. This arrangement can be influenced by ageing and disease, urging the understanding of normal and deviant morphological patterns down to the nanoscale level, as much as the exploration of techniques able to grant that knowledge. Here, the ultrastructure and composition of seven samples taken from the femoral neck cortical bone of a single donor (52 y.o. female, no metabolic bone disease) is assessed with emerging characterization techniques. Laboratory-based nanoscale X-ray computed tomography providing ~50 nm spatial resolution at $(16\ nm)^3$ voxel size resolves not only the lacuno-canalicular network but also the mineral ellipsoids associated with mineralized collagen fibrils (MCF). Site-matching 3D data with quantitative polarized Raman spectroscopy provides, in turn, complementary information on relative mineral and organic composition, while both techniques allow to quantify the MCF orientation. Bone matrix composition and lacuna-canalicular network organization are shown to vary between the osteonal and interstitial zones. Both plywood and gradual oscillating motifs of bone lamellation are observed, in line with existing theories. By combining these two methods, future studies can concentrate on other bone ultrastructural units of interest like interlamellar and cement interfaces, the structure of MCF around lacunae and near Haversian channels, as well as the influence of metabolic diseases on bone ultrastructure.

* Corresponding author at: ARTORG Center for Biomedical Engineering Research, University of Bern, Freiburgstrasse 3, 3010 Bern, Switzerland.
** Corresponding author at: Graz Center for Electron Microscopy (ZFE) and Institute of Electron Microscopy and Nanoanalysis (FELMI), Graz University of Technology, Steyrergasse 17, A-8010 Graz, Austria.
*** Corresponding author at: Institute of Micro- and Nanostructure Research (IMN) and Center for Nanoanalysis and Electron Microscopy (CENEM), IZNF, Friedrich-Alexander-Universität Erlangen-Nürnberg, Cauerstr. 3, 91058 Erlangen, Germany.
**** Corresponding author at: Empa, Swiss Federal Laboratories for Materials Science and Technology, Laboratory for High Performance Ceramics, Überlandstrasse 129, 8600 Dübendorf, Switzerland
E-mail addresses: tatiana.kochetkova@unibe.ch (T. Kochetkova), tatiana.kormilina@felmi-zfe.at (T. Kormilina), erdmann.spiecker@fau.de (E. Spiecker), jakob.schwiedrzik@empa.ch (J. Schwiedrzik).
[1] These authors contributed equally to this work.

https://doi.org/10.1016/j.actbio.2025.03.045
Received 23 November 2024; Received in revised form 23 February 2025; Accepted 25 March 2025
Available online 26 March 2025

Statement of significance: This study provides new insights into bone hierarchical organization, revealing local composition and lacuno-canalicular network organization within osteonal and interstitial bone zones, as well as their mineralized collagen fiber (MCF) orientation within the lamella. Synchrotron-like resolution was achieved on a laboratory-based nano-CT by exposing the volumes of interest from the bulk sample and applying machine learning segmentation algorithms. Site-matched analysis with quantitative Polarized Raman spectroscopy (qPRS) provided indirect access to relative mineral and organic composition variations and local MCF out-of-plane angle, with good agreement between the two methods. The proposed correlative experiment workflow greatly facilitates the characterization of bone ultrastructure and can be applied to other fields dealing with ordered hierarchical materials of similar feature sizes.

1. Introduction

Bone is a complex biological nanocomposite, combining toughness and strength with a low weight. Such remarkable material properties are characteristic of nature's hierarchical materials and are driven by the complex arrangement of their constituents from macro- down to the nanoscale [1–5]. Advances in characterizing these materials are crucial for understanding and mimicking their properties.

The material properties of bone are explained by its evolutional adaptation to provide mechanical support and organ protection in vertebrates. In bone, inorganic components primarily govern stiffness and compressive strength, while organic fraction promotes flexibility and toughness [6–8]. However, it is the hierarchical arrangement of the bone constituents that gives rise to its outstanding combination of mechanical properties [9]. This hierarchical complexity of bone tissue along with other natural materials has been a beacon of knowledge and inspiration for material scientists [10,11]. Adapting bone structure solutions to bio-mimetic man-made materials is a successful strategy throughout many research fields, including examples like bone anisotropy-driven hierarchical scaffolds for biomedical engineering [12], osteon- or compact/spongy bone-inspired composites for energy storage [13] or human femur loading patterns in civil engineering and architecture [14].

At the macroscale, cortical and trabecular types of bones can be distinguished. Cortical bone plays a prominent role in defining the overall tissue mechanical properties [15]. It forms the hard exterior (cortex) of bones, which is found on almost all bone surfaces, accounting for approximately 80 % of the total mass of the human skeleton [6]. In humans and other large mammals, cortical bone volume is permeated with cylindrical structures called osteons, typically 150–250 μm in diameter [16]. Interstitial tissue surrounds osteons and is composed of fragments of older osteons with higher mineralization [17,18]. Each osteon is made of concentric coaxial layers about 3–7 μm thick, called lamellae, that encompass the central canal – the Haversian canal. Blood vessels and nerves travel through this canal to supply the osteocyte cells with nutrients. Osteocyte cells reside inside lacunae, distributed within the volume of osteons, they connect through canaliculi, forming an extensive lacuno-canalicular network (LCN). Bone lamellae consist of stacks of sheets made of aligned mineralized collagen fibrils (MCFs), about 30–300 nm in diameter. MCF is often referred to as a main building block of bone, made of staggered collagen molecules with intra- and extra-fibrillar inclusions of hydroxyapatite (HA) crystals. Thereby, at the lowest scale bone is made of mineral crystals (HA, 50–60 wt. %), proteins (mainly collagen type I, 30–40 wt. %), and water [19–22].

The lamellar arrangement of cortical bone has been extensively studied for over a century [22–30], yet there is a lack of knowledge on the sub-lamellar organization of bone and its evolution with age or in the presence of a metabolic disease. Two models have been proposed to describe the bone lamellae organization. The first follows the work of Gebhardt [23] and states that bone lamellae are made of densely packed and aligned MCFs layers. Based on the predominant MCFs orientation pattern within the lamellae, three types of morphology can be distinguished: (1) longitudinal or (2) transverse (aka dark and bright lamellae) [31], where the principal MCFs orientation is parallel or orthogonal to the osteon main axis, respectively, and (3) alternating, where MCF orientation interchanges between transverse and longitudinal to the osteon axis [32–34]. According to the second model of Marotti [35], the bone lamellae have an interwoven texture of the MCFs and the bone lamellation appears due to the alteration of collagen-rich (dense) and collagen-poor (loose) lamellae. In its turn, a lamellar unit is thought to be a composite of ordered (dense) and disordered (loose) materials made of mineralized collagen fibrils with different degrees of alignment [22,30,36]. Despite the experimental evidence for both bone lamellation patterns, Gebhard's model is the most largely accepted.

Through the recent advances in biomedical imaging, various techniques have been used to assess bone's ultrastructure organization. These methods could be classified as light-based (polarized light microscopy, polarized Raman and Fourier transform infrared spectroscopy, polarized second harmonic generation, confocal laser scanning microscopy), X-ray-based (small- and wide-angle X-ray scattering (SAXS, WAXS); X-ray computed tomography), and electron-based (electron diffraction, electron backscatter diffraction; scanning and transmission electron microscopy (SEM, TEM)) [20]. Besides imaging, a quantitative assessment of the 3D ultrastructural organization is key to the understanding of structure-function relationships in bone tissue. However, only a few of the abovementioned techniques are suitable for this purpose, namely: synchrotron phase-contrast X-ray nanotomography [37,38], ptychography [39,40], SAXS and WAXS tensor tomography [41–43]. Moreover, serial sectioning using focused ion beam SEM (FIB-SEM) [22,44], electron tomography [45–47] and atomic probe tomography [48] techniques provide the highest imaging resolution but the last two operate on small volumes that are insufficient for statistical quantitative analysis, while FIB-SEM sectioning is inherently destructive. Still, both methods require the high brilliance of synchrotron radiation, causing sample degradation [49]. Today, synchrotron resolution capabilities can be reached using laboratory nanoscale X-ray computed tomography (nano-CT), entering a more cost-effective technique where the queues for high flux beamline time are replaced by slower in-house measurements with the laboratory X-ray sources. With a spatial resolution down to 50 nm and lower radiation doses, Zernike phase-contrast nano-CT yields high potential for the reproducible nanostructural analyses of natural and engineered biomaterials. This emerging technology has never yet been applied to cortical bone but was used, e.g., in a study of crack propagation in elephant tusk dentin [50].

Another technique, relevant for bone ultrastructure characterization is polarized Raman spectroscopy (PRS). As was shown recently, following careful calibration, this technique can be upgraded to quantitative PRS (qPRS), applicable for the quantitative 3D analysis of bone MCF orientation [51], besides the usual information on the bone organic and mineral composition at a sub-micron resolution. Raman techniques have shown great potential for clinical use when it comes to bone tissue. There have been many developments of spatially offset Raman spectroscopy (SORS) for *in vivo* determination of bone strength and composition [52] going as far as showcasing a proof-of-concept clinical setup used subcutaneously and on surgically exposed bone on live human subjects [53].

In the current work, we combine qPRS with the unique capabilities of a laboratory-based X-ray Zernike phase-contrast nano-CT using the state of art 3D data processing tools with machine learning algorithms to

collect a vast quantity of data on the MCF orientation. Following previously presented proof-of-concept for correlative study of intersecting measurement regions [54], we aim to quantitatively assess and verify the complex interplay between composition and 3D ultrastructure of cortical bone down to the sub-lamellar level.

2. Materials and methods

2.1. Human cortical bone samples

Human cortical bone samples were extracted from a single femoral neck slice, previously collected during total hip arthroplasty at the University Hospital of Bern [55] (Ethical approval 2018-01815, Kantonale Ethikkommission Bern). The bone donor (52 y.o., female) had no reported bone-related diseases. The femoral neck slice was mechanically cleaned with a scalpel, further cut with a diamond band saw under constant water irrigation (Exakt, Norderstedt, Reichert-Jung), and cleaned additionally with a water jet (Braun Oxyjet). Two bone samples (further referenced as samples A and B) were cut from the mid-cortex region of the femoral neck, from the inferior quadrant. Each of the samples had a hexahedral shape with approximately 3 mm × 3 mm surface area and 3–5 mm side length, matching the direction of the femoral neck main axis (schematically shown in Fig. 1). Samples were left to dry in a desiccator overnight, then glued into specially designed aluminum SEM stubs with a 2-component epoxy resin adhesive (Schnellfest, UHU, Germany). No chemical sample fixation was used. Protruding square side of the sample was polished with progressive grades of silicon carbide paper and finished manually on a soft cloth with a 1 µm diamond suspension followed by 0.04 µm SiO_2 suspension.

Free-standing bone micropillars were fabricated on the polished sample surface using ultrafast pulsed laser ablation [56]. A femtosecond laser system (SATSUMA HPII, Amplitudes Systemes) with 515 nm laser wavelength and a pulse repetition frequency of 3 kHz was used. With the maximum output laser power of 2 W, the resulting pulse energy and peak fluence were approximately 3.96 µJ and 5.14 J cm^{-2}, respectively. Micropillars were fabricated at the scanning laser mode, where the zones without ablation corresponded to the micropillars volumes. 2 × 2 pillar arrays were fabricated on each of the two bone samples. However, one micropillar from sample B was lost due to the underlying Haversian canal. As a result, 7 micropillars were used in this study as listed in Table S1, Supporting Information. The average pillar diameter and height were approximately 25 µm and 60 µm accordingly with ~14 ° taper. To remove the material redeposition after laser ablation, the bone samples were cleaned in an ultrasonic bath with NaCl solution (9 g l^{-1}) for approximately 30 s and dried later at room temperature.

2.2. Nanoscale X-ray computed tomography

Prior to tomography acquisition, micropillars were decorated with gold microparticles (Alfa Aesar 0.8–3.0 µm, 99.96+ %) acting as fiducial markers for the alignment software of the microscope as well as for future position matching tasks. Reference light microscopy (LM) images of gold particle positions were acquired using Nikon Eclipse LV100ND. Samples were placed in the optical path of the nano-CT microscope several hours prior to the experiment to suppress the sensitivity of bulk base to room humidity levels and consecutive drift during tomography acquisition.

The nano-CT experiments were performed with a ZEISS Xradia 810 Ultra laboratory-scale X-ray microscope. It is equipped with a 5.4 keV rotating anode Cr source and operates with quasi-monochromatic X-rays at constant photon energy with parallel beam geometry. A phase contrast regime introduces a phase ring in the beam path after the objective. The phase ring shifts the phase of the background light relative to the light scattered by the specimen. The interference of the two beams in the detector plane turns phase shifts into intensity variation, which enables Zernike phase contrast imaging [57,58].

All the nano-CT data volumes in this study were acquired using the Zernike phase contrast regime in high-resolution (HRES) mode associated with a field of view of 16 µm × 16 µm with an optical resolution down to 50 nm. Data was acquired at 16.09 nm pixel size with exposure time of 180 s per projection. For some samples, several tomography volumes were recorded and stitched during post-processing. Details on nano-CT measurement conditions for different samples can be found in Table S1, Supporting information. Direct positions of measurements

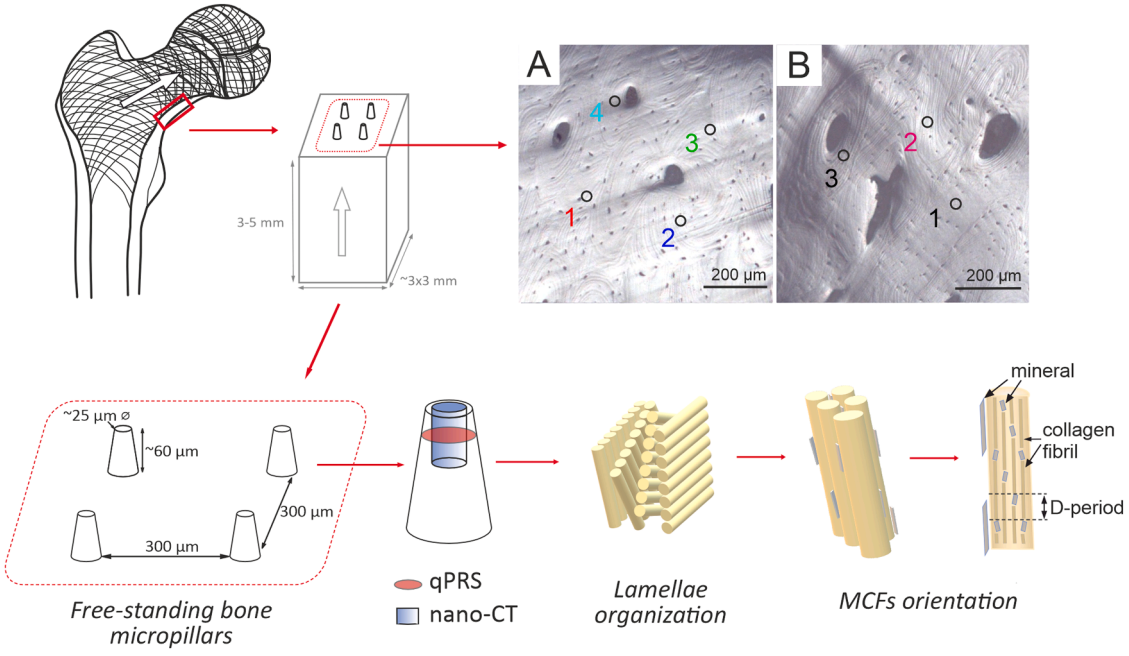

Fig. 1. Cortical bone samples were extracted from the middle region of the inferomedial femoral neck quadrant, and free-standing bone micropillars were prepared using femtosecond laser ablation. Positions for resultant volumes of interest are marked on the light microscopy images showing the original surfaces of the bone samples (A, B). Within the volume of bone micropillars, quantitative Polarized Raman Spectroscopy (qPRS) maps were collected together with the nano-CT. Combination of the two techniques gives assess to the bone tissue composition as well as lamellae organization and mineralized collagen fibrils (MCF) orientation.

compared to qPRS sites are displayed in Figure S6, Supporting Information.

Nano-CT data collection exposes the sample to the X-ray radiation. Here, samples were continuously exposed to 5.4 keV at 0.9 kW power for up to 75 h during a single measurement. In spite of that, we have not observed known radiation damage markers (browning, micro-cracking) or any considerable differences in first/last taken nano-CT projections, nor in the common area of two intersecting nano-CT measurements of samples A2 Indigo and A3 Green taken several months apart. The control Raman spectra taken before and after the nano-CT measurements have not indicated any sign of collagen cross-linking suggested by literature on X-ray radiation damage [49].

All collected tilt series were aligned using the adaptive motion compensation procedure (AMC), implemented in the native acquisition software (ZEISS XM-Controller) [59]. All volumes were individually reconstructed with the same parameters using the in-house Python script based on Astra Toolbox [60] utilizing the simultaneous iterative reconstruction technique (SIRT) algorithm. Reconstruction results in a stack of virtual horizontal slices through the recorded object volume.

Nano-CT scans were collected from four VOI in sample A and one volume from sample B (pillar 2). Throughout the text, we implement sample notation in a form 'A1 Red' etc. composed of Sample (A/B) + VOI# (1–4) + Color (Red/Indigo/Green/Cyan/Magenta) according to Fig. 1 in order to ensure traceability through different graphic representations. See Table S1, Supporting Information, for details.

2.3. 3D data processing

The main software used for 3D data handling was Arivis Vision4D, version 3.3.0 (further on Arivis). Arivis plots 3D data using a right-hand extrinsic ZYX coordinate system (XY is the horizontal plane of the main slice direction for the dataset and Z is the direction of the stack). The software offers a *Transformation Gallery* operation to change the direction of the main slice plane. Reconstructed horizontal stacks were thus imported and resliced into a stack of vertical slices parallel to assumed femoral neck axis where the anisotropic character of material contrast was best observed (in a common XY plane orientation for all pillars in sample A and in an arbitrary chosen for B2 Magenta).

For samples A2 Indigo and A4 Cyan, vertical slice stacks of two overlapping tomography volumes were white-balanced using ImageJ and stitched manually using a *Tile sorter* import function in Arivis Vision4D software. A2 Indigo joined volume has also been stitched to a third acquired tomography volume (see Table S1, Supporting Information) for extended LCN representation in Video SV2, Supporting Information. *Tile sorter* is a rather rudimentary stitching solution, and it has resulted in a certain level of edge artifacts in the overlap region; at the same time, extending the investigated volume proved very insightful in studying the lamellar structure and LCN propagation.

2.4. Segmentation

Manual segmentation of the lamellar volumes was conducted by visualizing the contrast evolution while navigating through the 2D slices. An orientation of vertical slicing was found that appeared orthogonal to these changes as shown in Videos SV3–5, Supporting Information. Corresponding areas were traced using *Draw objects* tool, and thus-defined sub-volumes of the bone were separated using the drawn objects in a *Mask* operation.

Segmentations of nano-CT volume in order to isolate structures of interest were impeded by the inhomogeneity of bone material and resulting fluctuations in contrast levels throughout the 3D volume rendering intensity thresholding-based methods impossible. This hurdle has been overcome by using *Machine Learning* functionality of the Arivis software that employs the Random forest algorithm based on the open source tool Ilastik [61]. The LCN for all the samples have been segmented at the default *'Fluorescence and EM Robust'* preset. Since several spaces between mineral ellipsoids had comparably low intensity levels, it has been challenging to distinguish between these areas of low mineralization, laser ablation pores and parts of discontinuous canaliculi. In the LCN reconstructions, only the thin channels having a visible connection to a bigger canaliculus were kept.

For MCF segmentation (or rather for the segmentation of co-oriented mineral ellipsoids), we chose a custom *'Orientation'* feature-based mode of the tool to encourage the choice of elongated objects. Teaching was performed separately for each dataset and segmentation parameters of *(acceptance) Threshold* and *Smoothing* were chosen individually to achieve the best representation. The discoverability of fibril segments is heavily influenced by the teaching examples, intensity values of the dataset and the angle between the slice plane and true lamella plane. In case of lamella-segmented datasets, the same segmentation training and parameters were used to compare MCF orientation between the lamellar volumes.

The error of segmentation and orientation determined by the software was assessed using a Python-generated 3D phantom with known orientations as commented in Supplementary chapter S11, Supporting Information.

2.5. Quantitative polarized Raman spectroscopy

Raman spectroscopy is a non-destructive method used to probe the local tissue composition. It relies on collecting inelastically scattered (Raman) photons from the specimen upon excitation. By incorporating a polarizer into the system and performing careful calibration, the spatial orientation of the molecules can be estimated based on the anisotropic spectral response. The resulting quantitative polarized Raman spectroscopy (qPRS) method enables not only the traditional characterization of tissue composition but also offers quantitative insights into the orientation of MCF. qPRS measurements were performed on each bone pillar surface, ~5 μm underneath the pillar top. Raman spectra were acquired using a confocal Raman microscope (WITec Alpha 300 R) in backscattering geometry. Linearly polarized 785 nm laser at 30 mW power was used in combination with 50× objective (0.80 numerical aperture), resulting in a laser spot of ~1 μm in diameter. Spectra were registered using 400 mm lens-based spectrometer with a 300 g mm^{-1} grating equipped with a cooled deep-depletion CCD. qPRS measurements were collected at different excitation polarizations from 0° to 180° with a 10° polarization angle step and 30 s integration time, resulting in 19 polarized Raman spectra per measurement spot. On each bone pillar, a qPRS map was collected, consisting of a 5 × 5 (9 × 9 for sample B) grid of measurement locations with a 3.5 μm step (1 μm step for sample B).

The following Raman parameters were collected from each location:

1. in-plane and out-of-plane orientation angle of mineralized collagen fibrils, estimated from the spectral anisotropy of amide I and III bands following the previously established methodology (see Supplementary chapter S8 in the Supporting Information and [51] for more details);
2. mineral to matrix ratios, estimated from the Raman band integral area ratios of primary phosphate (ν_1PO_4, 920–990 cm^{-1}) over collagen amide I band (1570–1740 cm^{-1}). Ratios were estimated at each laser polarization and the mean value was taken, avoiding possible effects of the polarization [62];
3. mineral crystallinity was assessed from $FWHM^{-1}$ (inverse value of full width at half maximum) of the ν_1PO_4, fitted at each laser polarization and the mean value was taken, avoiding possible effects of the polarization;
4. to assess the collagen quality, the ratios of amide I (1640/1670 cm^{-1}) and amide III (1245/1270 cm^{-1}) sub-bands were collected, as proposed by Unal et al. [63,64]. Again, ratios were estimated at each laser polarization and the mean value was taken, avoiding possible effects of the polarization.

Raman spectra processing was done using Python v3.8 [65]. Detailed description of the spectra processing steps can be found in the Supplementary chapter S8, Supporting Information.

2.6. ROI and MCF angle correlation analysis

Due to the different physical principles of the nano-CT segmentation and qPRS calculations, extensive measures were taken to combine and compare the results of both, including the measurement position correlation and transformations to the common coordinate system.

Raman datapoint positions are tied to pixel coordinates of LM images. In their turn, objects segmented in nano-CT analysis are defined by voxel coordinates in nano-CT reconstruction. In horizontal plane their positions can be described by pixel positions in a horizontal virtual slice. These positions were matched following the description in Supplementary chapter S5, Supporting Information, using LM reference images of micropillars decorated with gold nanoparticles. Features such as gold particles and pillar edge perimeter were used to align the images determining the position and orientation of nano-CT dataset. Based on this relationship, a series of MATLAB scripts [66] were utilized to compute and manipulate position data of measurement and segmentation.

The intersecting information of both measurements was found by selecting the MCFs segments from the nano-CT scans fully or partially located at the extended volumes of qPRS measurement. qPRS measurement points were approximated as parallelepipeds with acceptance parameters ε_{XZ} and ε_{Y}. Expected lateral resolution of qPRS measurement is ~1 μm and depth resolution <2 μm. Since MCF are expected to keep their orientation on the length scales much extending theses and for better statistical representation, we set both ε_{XZ} and ε_{Y} acceptance ranges at 2 μm.

For the correlative analysis of the MCFs angles, both measurements were transformed into the right-hand Tait-Bryan angle notation [67], where in-plane rotation is characterized by angle $\psi \in [-\pi,\pi]$, and out-of-plane rotation is characterized by angle $\theta \in [0,\pi/2]$. MCFs were considered as cylinders, possessing radial symmetry, the rotation (φ) around the main MCFs axis is irrelevant for our measurement. For performing averaging and statistics of orientation data achieved from segmentation, a *MATLAB Circular statistics toolbox* [68] has been implemented.

The details of translation operations between coordinate systems and angular notations of individual measurements are given in Supplementary chapter S5, Supporting Information.

2.7. Statistical analysis

Statistical analysis was done in R version 4.3.1 [69], *rstatix* package [70]. Compositional comparison between the two cortical bone zones was done via the two-tailed *t*-test, following the Shapiro-Wilk normality test. Correlative analysis between the out-of-plane MCFs angles assessed via qPRS and nano-CT was done through the linear regression analysis (*lmtest* package) [71].

3. Results and discussion

3.1. Bone tissue appearance in nano-CT

Investigated bone volumes were located on two cortical bone samples, prepared from a single human femoral neck slice. The volumes of interest (VOI) were exposed from the bulk sample using femtosecond laser ablation, leaving the freestanding microscale bone pillars (Fig. 1) with an approximate height of 60 μm and diameter of 25 μm. Removing surrounding bulk tissue allowed us to isolate the VOI and increase the quality of nano-CT measurement by avoiding interior tomography artifacts.

Reconstructed virtual cylindrical volumes of 16 μm in diameter and 16 μm in height were resliced vertically, parallel to the assumed femoral neck axis (XY plane). Videos SV1–5, Supporting Information, demonstrate the resulting XY planes for each of the samples. In these slices, as well as in Fig. 2B, appearing dark voids with bright halos (marked in dashed circles in Fig. 2B) are the traversing canaliculi channels, which will be discussed in the next section.

In addition to that, the XY slices through the nano-CT reconstruction exhibit a contrasting pattern given by bright elliptical features that seem to have a preferred orientation. Fig. 2A-B demonstrates two orthogonal planes, sliced as indicated in Fig. 2A. The patterns seen in XY and ZY planes have been termed as a “filamentous motif” (Fig. 2D) and “rosette (orthogonal) or lacy (intermediate) motif” (Fig. 2C) by Reznikov et al. [72]. By now these motifs are known to compose together three-dimensional prolate ellipsoidal (or marquise-shaped) [73] mineral clusters [74] of nanosized apatite crystal platelets (also called mineral ellipsoids [75], spherulites [76] or tesselites [77] by different authors) that accompany mineralized collagen fibrils.

It is generally accepted that the long axis (crystallographic c-axis) of mineral ellipsoids is co-oriented with the MCF, as concluded from various scattering techniques [78] and evident from TEM studies [79].

A characterization of mineral ellipsoids themselves has not been a goal of the present study. At the same time, a statistically relevant amount of data has been acquired on their respective morphological parameters throughout the various segmentations (see Materials and Methods). An interested reader is invited to follow this data in Supplementary Chapter S3, Supporting Information. In summary, for the mineral ellipsoid size, we record mean values measured over several thousands of objects as 842±412 nm for the length and 428±205 nm for the largest orthogonal diameter (Table S3, Supporting Information).

Previous studies of mineral ellipsoid size show broad distribution of values. Shah et al. have measured around 300 marquise-shaped mineral clusters in deproteinized rat cranium as seen in SEM images to lay in a size range of 0.6–3.5 μm in length and 0.2–1.5 μm in diameter [73]. A review study of “rosette” cross-sections performed through numerous high-angle annular dark-field scanning transmission electron microscopy (HAADF-STEM) images capturing human bone in femur, spine and maxilla regions has identified 83 structures with the sizes ranging from 101 to 1187 nm with an average size of 692±196 nm [75]. With the development of 3D measurement techniques and corresponding analysis tools, volume segmentations of these structures became possible. Buss et al. demonstrated very elaborate segmentation results of thousands of tessellated ellipsoids from a FIB-SEM serial sectioning of mouse tibia, reporting sizes of 2–2.5 μm length and 0.5–1 μm diameter in healthy mice [77]. At the same time, available 3D data of mineral ellipsoids in human bone is not as statistically rich. Binkley et al. have measured the sizes of 8 ellipsoids recognized from FIB-SEM serial sectioning of human femur [74]. Values there vary between 850 and 1575 nm for the length and 450 to 875 nm for the widths averaging at 1.1 μm of length and 700 nm of maximal diameter. HAADF-STEM tomography of a TEM lamella, included in the abovementioned work of Micheletti et al., presented three mineral ellipsoids with diameters of 306, 363 and 632 nm [75]. There is no doubt that the ellipsoids discussed in our study are the same structural features as described in abovementioned works. There is also a good agreement between the aspect ratios reported. Ours of 2.03±1.39 is very close to 2.05 of Buss et al. [77] and comparable to ~2.4 reported by Shah et al. [73].

There is a practical explanation for generally lower size values resulting from our segmentations. Mineralization studies have shown ellipsoids to grow out of their dense center as distinct structures, then tesselate and connect into an interwoven mesh [73,77]. Whereas most other authors have done their calculations on the tissue at the early stages of mineral apposition with discrete ellipsoids in view, our investigated bone volumes would be at the later, completely interwoven stage characteristic of the skeletally mature donor [73], where ellipsoid boundary contrast is obscured and smeared by interconnected mineral matrix. Nano-CT measurements operate at a resolution much inferior to

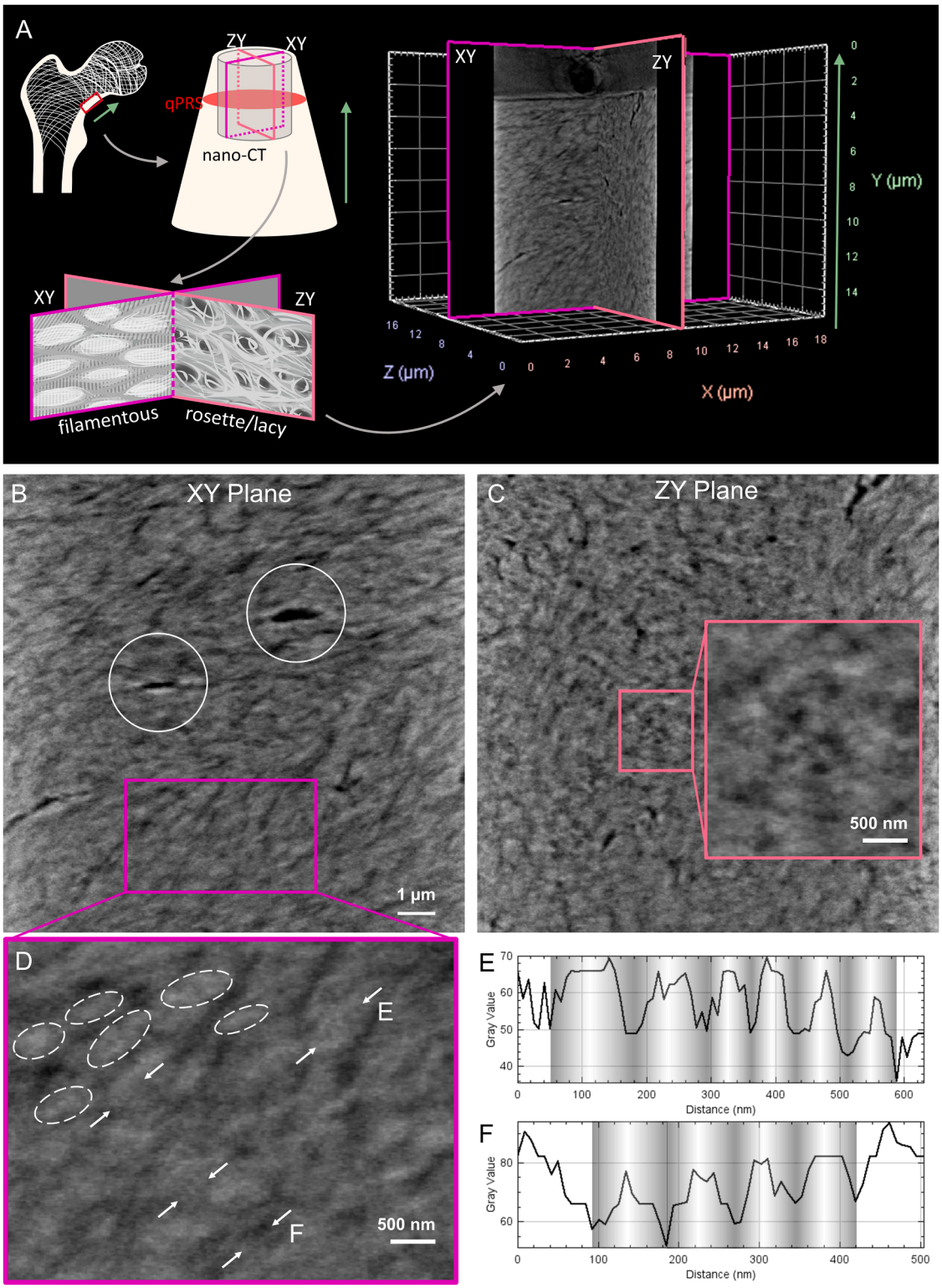

Fig. 2. Nano-CT slices of B2 Magenta in two orthogonal planes (XY and ZY) oriented following the sketch in (A). Green arrow marks femoral neck direction. Two orthogonal planes are shown in subfigures (B) and (C). Solid circles (B) are marking canaliculi voids. Inset in subfigure (C) reveals a rosette motif; the framed region from (B) enlarged in (D) reveals aligned elliptical features (traced in the upper left corner by a dashed line) and visible periodical intensity fluctuations in areas marked with arrowheads. Line intensity profiles taken between arrowheads (E) and (F) are shown in respective subfigures, the mean period is 83±26 nm.

that of electron microscopy and cannot define a fine boundary of nanoscale mineral platelets composing the ellipsoids. Thus, where other authors pursued to capture the precise morphology of the ellipsoids, we were only interested in their orientation. Consequently, we have kept our segmentation *(acceptance) Threshold* parameter rather high to select the feature boundary slightly smaller than estimated by operator, in order to avoid false recognition and to have better chances of separating individual objects in the full volume. For estimating the difference in approach, one can compare the selection in Figure S3, with only the bright core of an ellipsoid being approved, to the complete area

coverage in Figs. 4–5 of Buss et al. [77].

The interfibrillar mineral within the MCF is arranged periodically within the gaps of collinear collagen molecules, creating the characteristic gap and overlap regions at a 67 nm periodicity, known as the D-spacing period of the collagen fibril [80]. Normally, the expected D-spacing period of collagen would be at the very limit of the nano-CT nominal resolution (50 nm). However, as a closer inspection of parameters at play has shown [81], the oversampling at $(16\ nm)^3$ voxel size with good quality reconstruction (Simultaneous Iterative Reconstruction Technique, SIRT) allows to distinguish features separated by lesser distances. Additionally, Zernike phase contrast enhances morphology contrast, which helps indicate the intensity pattern even when the individual spacing stays at the edge of the resolution limit. In some areas of lamella-oriented virtual slices (see areas between arrowheads in Fig. 2C), the intensity variation along the long axis of the elliptical features suggests the possible D-spacing pattern. Typical line profiles through such intensity fluctuations are given in Fig. 2D and E. As measured over 47 minima through 7 recorded profiles (Figure S2, Supporting Information), a mean periodicity of 83±26 nm is observed, which is in rough agreement with the expected D-spacing period of 67 nm given the 16 nm pixel size.

Consequent to these considerations, we hereafter assume that the mineral ellipsoids are intimately connected to collagen fibrils, presumably overlapping or enclosing in them, and further recognize their orientation as that of MCF. Other X-ray studies following the same hypotheses [38] have achieved the results of MCF orientation in good agreement with those established on demineralized samples [82].

3.2. Structural and compositional variation between interstitial and osteonal zones

As can be seen in light microscopy images in Fig. 1, and sketches of magnified pillar positions in Fig. 3, examined bone volumes include both osteonal and interstitial regions. Pillars 2 and 4 from Sample A (A2 Indigo and A4 Cyan), as well as pillar 3 from Sample B (B3), are located within secondary osteons. Meanwhile, pillar 1 and 3 from Sample A (A1 Red and A3 Green) as well as pillar 1 and 2 from Sample B (B1 and B2 Magenta) are located inside interstitial bone regions, which consist of older osteonal tissue resulting from earlier bone remodeling cycles. On the scale of several micrometers, we observe distinct morphological differences between the probed bone volumes that are summarized in Table 1.

Zonal dependence is observed in lacuno-canalicular network (LCN) appearance within osteonal and interstitial regions (Fig. 3). LCNs in the individual pillar samples have been segmented from vertical cross-sectional slices of nano-CT reconstructions. Videos SV1–5, Supporting

Table 1
Summary of the observed differences between the interstitial and osteonal bone volumes.

		Interstitial	Osteonal
Lacuno-canalicular network	Appearance	Irregular orientation with a high degree of branching and kinking	High directionality
	Propagation	Along the femoral neck axis	Orthogonal to the femoral neck axis
Local composition	Crystallinity (v_1PO_4 $FWHM^{-1}$)	Higher	Lower
	Collagen disorder/order ratio (I_{1670}/I_{1640})	Higher	Lower

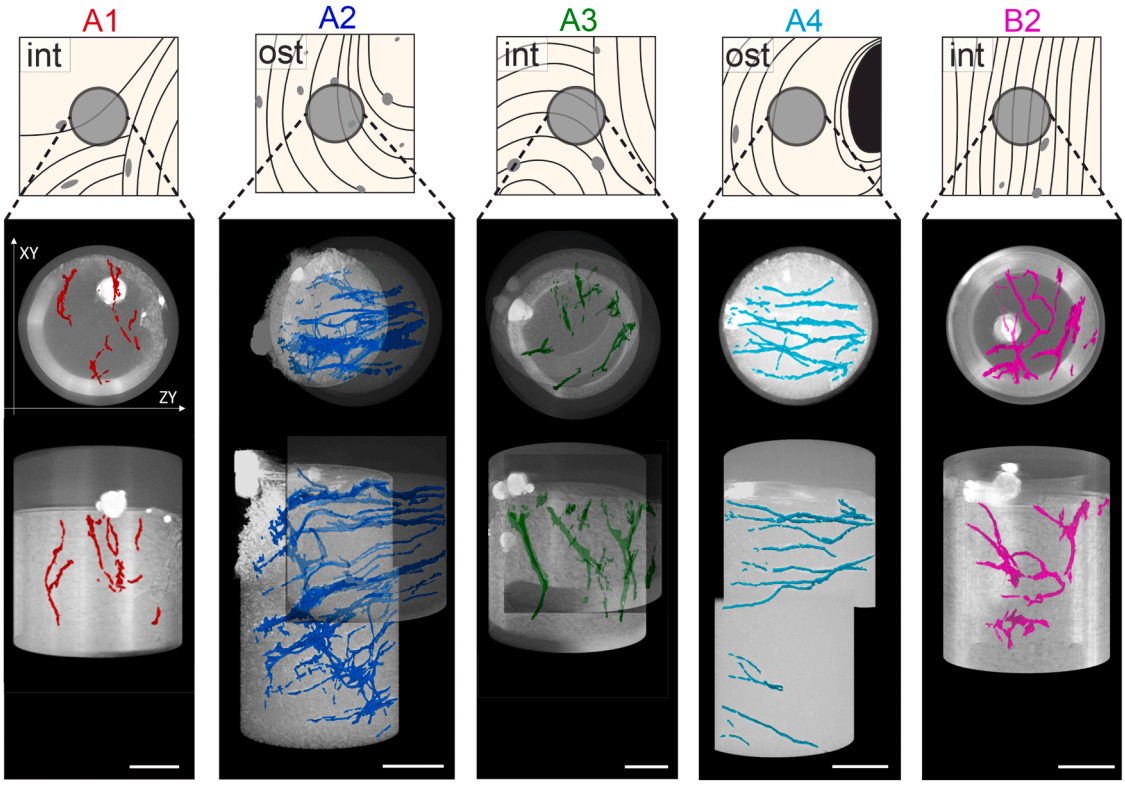

Fig. 3. The volumes of interest chosen within the interstitial (int) and osteonal (ost) regions of cortical bone samples, as marked on the upper sketch, created from the light microscopy images A and B, Fig. 1. The top views of the nano-CT volumes follow the orientation of the sketch, while the bottom views show the reconstructed volumes from the side and follow the presumed femoral neck main axis, with planar orientation in ZY (perpendicular to the presumed lamellar plane XY). For A2 Indigo and A3 Green, an overlay with a second dataset is used to demonstrate the extending LCN pattern. Scale bar is 5 μm.

Information demonstrate LCN rendering for each pillar sample, and the comparison between the different pillars can be seen in Fig. 3. Within interstitial regions of volumes A1 Red, A3 Green and B2 Magenta, the LCN demonstrates irregular orientation with a high degree of branching and kinking. Most canaliculi are thick and run along the femoral neck axis. In samples A1 Red, A3 Green, we observe several discontinuous broken canaliculi that may be examples of canaliculi pruning. It is reasonable to think that some channels would gradually degrade and dissolve with age, replaced by ongoing mineralization [83]. While our study focused on a mature bone sample (52 years old), incorporating data from younger patients or different loading scenarios [84] would offer valuable insights into the progression of LCN structural configuration.

The detected canaliculi in osteonal regions A2 Indigo and A4 Cyan appear orthogonal to the main axis of the femoral neck (Fig. 3). A4 Cyan demonstrates a vascularization pattern of several small canaliculi running in parallel, with their cross sections lying on the same circumference (Video SV4 Planes 300–600, Supporting Information). The high directionality of the LCN within the osteonal bone regions is in line with previous studies [36]. Following the work of Repp et al. [85], most of the osteonal canaliculi (about 64 %) are expected to be oriented towards the osteon center, while the lateral canaliculi lie parallel to the osteonal axis, often following the predominant MCF orientation of the lamellae.

Remarkably, the volume of a secondary osteon within the pillar A2 Indigo presents a dense canalicular network visible in the volume rendering in Fig. 3 *and* Video SV2, Supporting Information. Numerous canaliculi run perpendicular to the assumed femoral neck axis, while connected by a thick row of junction points. Junctions are comparatively small (in our case under 4 μm in diameter), connecting several branching strands of canaliculi. In contrast to such junctions, an osteocyte's lacuna in the case of human cortical bone is usually about 10–15 μm in diameter with hundreds of individual canaliculi sprouting from the lacunae volume [86]. Canaliculi junctions are reported as a common LCN feature in both humans and rodents [87]. Observed here pattern of an aligned row of canaliculi junction points appears extremely similar to the one observed by Reznikov et al. [82] in rat tibia. Bortel et al. [86] have classified the junctions in human bone, suggesting they serve the redundancy of nutrient transport in case of tissue damage, but have only considered junctions close to lacunae.

Polarized Raman spectroscopy further highlighted the zonal differences within cortical bone. In Fig. 4, a typical Raman spectrum of cortical bone as measured in the current study is shown. Raman bands that correspond to the mineral (v_1PO_4, v_2PO_4) and organic (amide I, amide III) components are marked accordingly. Relative mineralization is assessed via mineral to matrix band ratio v_1PO_4/amide I [63,88,89], averaged over different laser polarization [62]. As shown in Fig. 4A, the mineral to matrix ratio (v_1PO_4/amide I) is comparable between the osteonal and interstitial zones, suggesting that the investigated volumes underwent the bone formation cycle at similar points in time. Another parameter that characterizes the mineral fraction of bone is the mineral crystallinity. It is assessed as the inverse full width at a half maximum (FWHM) of the primary phosphate band, averaged over different incoming laser polarizations [88,90,91]. In line with available studies [55,92], crystallinity is significantly higher within the interstitial regions of bone when compared to the osteonal (Fig. 4B). In the latter regions, a wider distribution of crystallinity values is observed, suggesting varying tissue age within the studied osteons [93]. Raman bands corresponding to the organic fraction of bone gave access to the local MCF spatial orientation [51] as well as the relative measure of the collagen secondary structure orderliness [63,64]. Collagen disorder/-order ratio is extracted as the sub-band intensities ratio for both amide I (1670 cm^{-1}/1640 cm^{-1}) and amide III (1245 cm^{-1}/1270 cm^{-1}). The amide I sub-band ratio demonstrated a significant increase for the interstitial bone (Fig. 4C-D), suggesting a less ordered collagen fibril arrangement [55,63,64,89]. An overlay of the qPRS measurement outputs (out-of-plane angle, mineral/matrix ratio, amide I sub-bands ratio) over the measurement sites/positions are summarized in Figure S10, Supporting Information.

3.3. Lamellar structure and MCF orientation

Nano-CT data has provided us with two paths to gain insight into lamellar arrangement of bone material in the imaged volumes. The first one has offered itself upon the examination of nano-CT XY slices (an example of such slice is shown in Fig. 5A). As we virtually slice through the bone volume, we follow local areas where the material contrast visually appears to follow different propagation patterns than the area next to it. Although we have observed some indication of lamellar patterns in all five samples, we have chosen three volumes (A3 Green, A4 Cyan and B2 Magenta), where we were able to find a plane running through the areas of different material contrast, so that the position of the boundaries between areas remained unchanged. The boundaries between areas appeared as straight lines and roughly parallel to one another, likely to reflect the lamellar structure of bone, as indicated in Figs. 5A and E. The reader is invited to follow these changes themselves through Videos SV3 and SV4, Supporting Information, where we used the difference in propagation direction to segment samples into lamellar sub-volumes. Fig. 5A and E feature the orthogonal view of the proposed lamellar segmentation for A3 Green and A4 Cyan, featuring in each case 3 parallel lamellar volumes (LV) with both boundaries traceable through the slices as well as edge volumes (EV) of the dataset, extending outwards from the utmost left and right identified boundaries. Recognized layers lay at 9° inclination in case of A4 Cyan to an expected femoral neck main axis. In A3 Green, however, the layers lay at almost 45° The thickness of the LV layers is measured as 2.3 to 3.6 μm for A3 Green and 2.4 to 4.5 μm for A4 Cyan as reflected in Table 2.

The second path is laid out by the MCF orientation estimated from the orientation of segmented mineral ellipsoids in the nano-CT reconstructions (Figs. 5B,C,D,F,G). In the aforementioned cases of A3 Green and A4 Cyan, the orientation distribution of MCF angles seen in color-mapped 3D renderings seems to correlate with proposed lamellar division achieved by the first path. Fig. 5 and Videos SV3 and SV4, Supporting Information use a *'Spectrum'* color scale (Fig. 5C) to reflect the orientation of the segments respective to the XY plane of segmentation (XY angle measured clockwise from horizontal X axis as plotted in Fig. 5D). In A4 Cyan, color fluctuations between yellow (~ 30° to 50°) and green (~ 10° to 40°)-dominating areas resemble the identified lamellar layers. At the same time, the layers formed by color variations appear to be of equal width of roughly 3.2 μm (measured from 3D views) contrary to the span of 2.4 to 4.5 μm measured in segmented layers (first path described in the above paragraph). For the sample A3 Green, the 3D view in Fig. 5G suggests three layers based on color distribution, namely yellow-green (ca. 10° to 50°) corresponding to EV2 and LV3, purple-blue (~ −90° to −10°) corresponding to LV2 and LV1 and cyan (~ −30° to 0°) corresponding to EV1. Under closer inspection, yellow-green (~ 10° to 50°) layer at the edge of the pillar changes again to cyan (~ −30° to 0°), however, due to laser ablation damage at the edges, the orientation of segments there is less reliable. Statistics corresponding to MCF orientation are plotted in Fig. 5H and I and summarized in Table 2.

Observed bone lamellae motifs both in osteonal and interstitial zones confirm existing theories of bone lamellation [34,38,79]. For the osteonal tissue in A4 Cyan, we observed a subtle periodic variation with an amplitude of ~6.5° between the successive layers (Fig. 5B, C), somewhat similar to the local observations of Varga et al. [38] and Schrof et al. [94]. In contrast to these gradual oscillations, interstitial tissue in A3 Green demonstrates a drastic change in MCF orientation between LV2 and LV3, as evident both from color contrast in Fig. 5F, G and the segment statistic in Figure 5 I. Median angle values in these two layers are −26.2° and 29.7° suggesting a 55.5° switch in orientation (Fig. 5E, D), in line with the proposed spiral twisting of Wagermaier at el [34]. The angle change between EV1 and LV1 within A3 Green is less extreme. The co-existence of both twisting and oscillating plywood

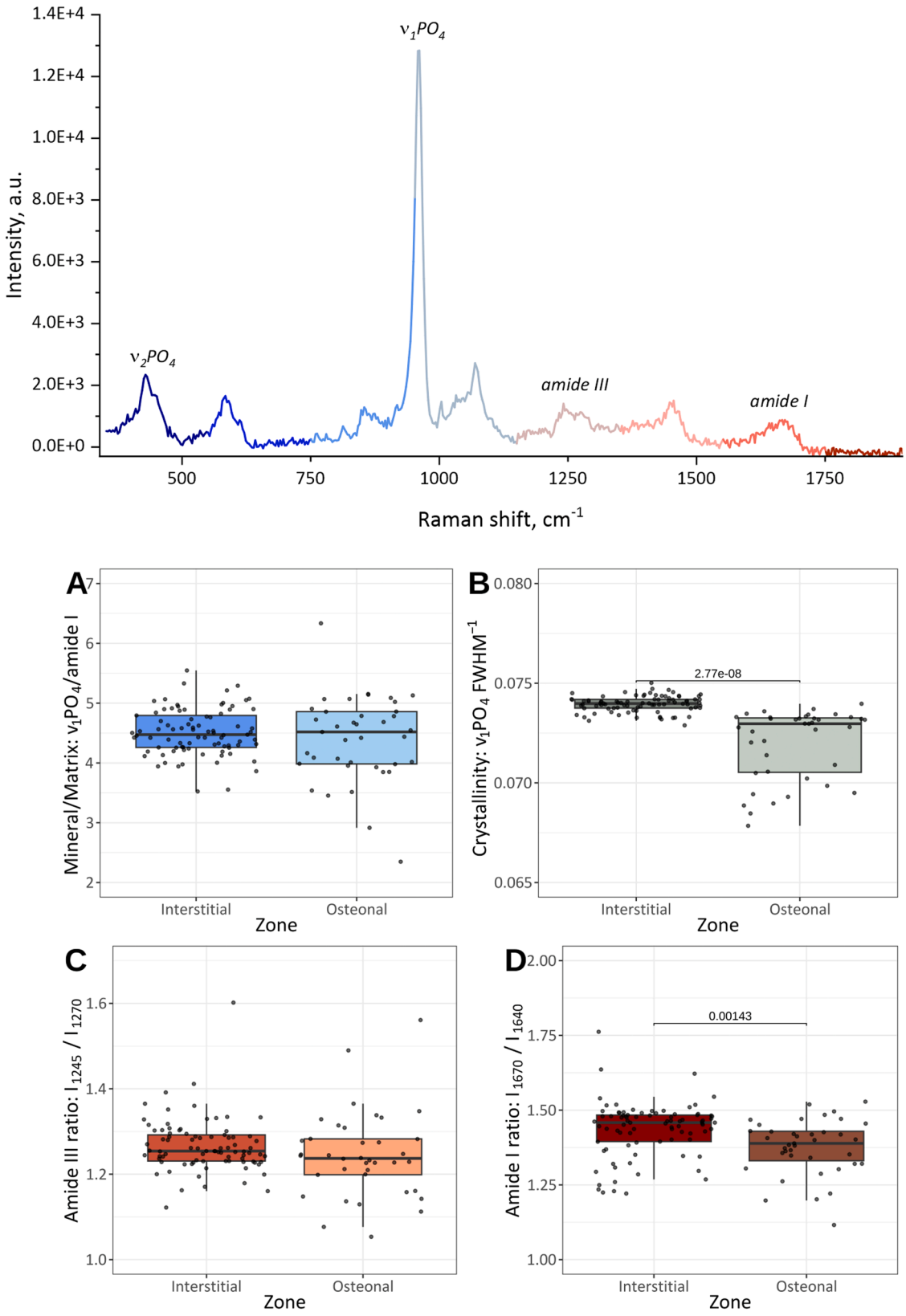

Fig. 4. Compositional comparison between the interstitial and osteonal zones as assessed via Raman spectroscopy. Top: representative Raman spectrum of cortical bone, coloring corresponding to different spectral regions, from which the following Raman parameters were extracted: mineral to matrix ratios (A), crystallinity (B), amide III (C) and amide I (D) sub-band intensity ratios. Boxplots (A-D) summarize the distribution of the Raman parameters within interstitial and osteonal zones, *p*-values from the two-tailed *t*-test are shown upon significant differences between the zones.

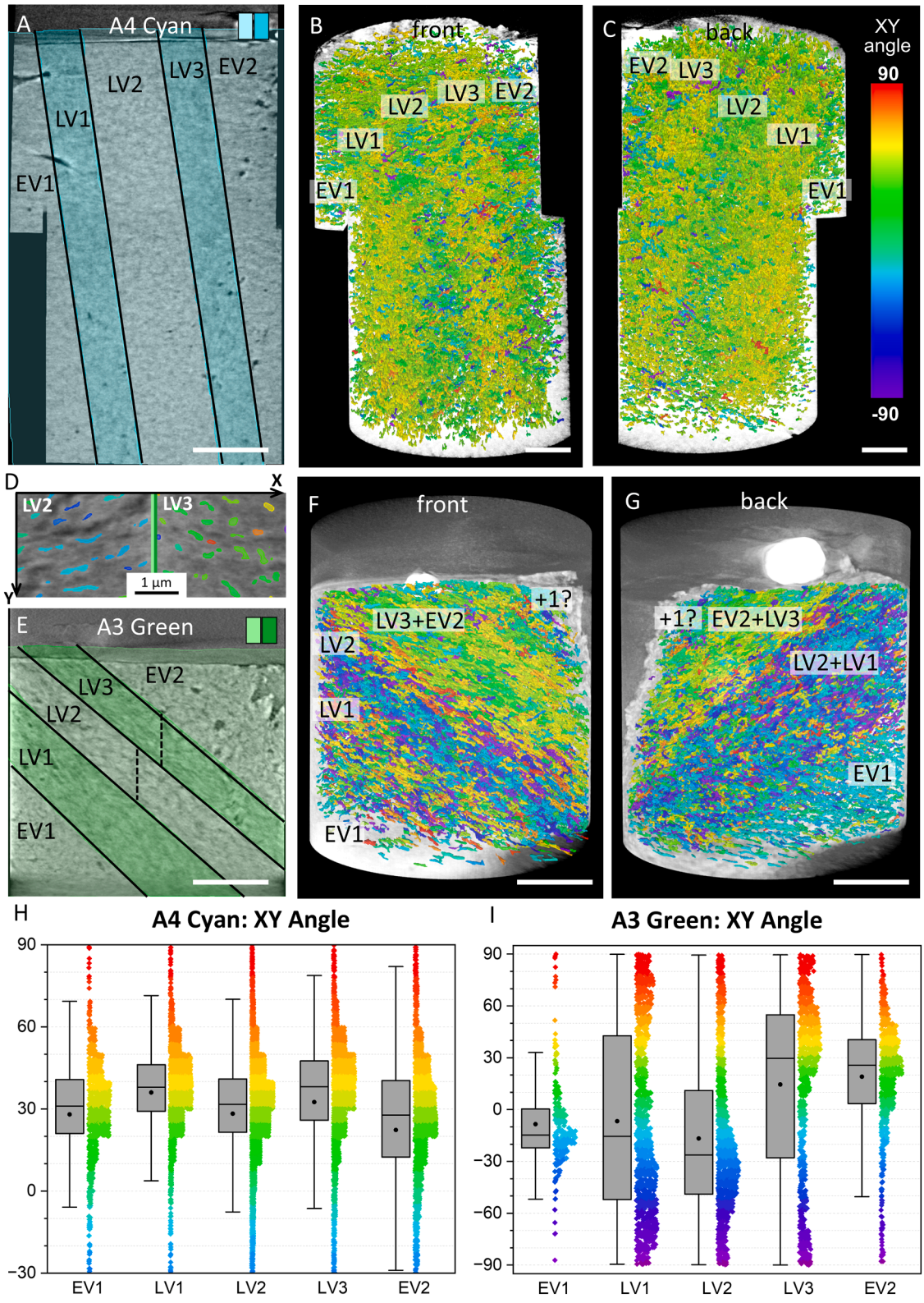

Fig. 5. Segmentation of lamellar structure. (A, E) - lamellar volumes (LV) and edge volumes (EV) identified following Videos SV4 and SV3 for samples A4 Cyan and A3 Green, respectively. (B,C) and (F,G) – 3D views of respective samples showing segment orientation in XY plane according to the color scale in (C; D) – Examples of 2D views in XY plane featuring a change of orientation between LV2 and LV3 in A3 Green; (H, I) – statistics of the segment orientation throughout the lamellar volumes; each is accompanied by a distribution histogram following the color scale from (C). Data is represented as a boxplot with median values marked by a line and mean values by a dot. Note different angle range of (H) and (I). Scale bars are 5µm.

Table 2
Summary on mineralized collagen fibrils (MCF) orientation within lamellar volumes (LV), edge volumes (EV) and half- layers (H-L), measured for A4 Cyan, A3 Green and B2 Magenta samples.

Sample A	Property	EV1	LV1		LV2	LV3		EV2
A4	MCF XY angle median [°]	31.0	37.9		31.7	38.1		27.8
Cyan	MCF XY angle mean [°]	28.0	36.0		28.3	32.5		22.3
	Lamellar thickness estimated from nano-CT slices [μm]	–	2.4		4.5	2.5		–
	Lamellar thickness estimated from color mapping [μm]	–	3.2		3.2	3.2		–
A3 Green	MCF XY angle median [°]	−14.7	−15.5		−26.2	29.7		25.7
	MCF XY angle mean [°]	−8.5	−6.7		−16.7	14.5		19.0
	Lamellar thickness estimated from nano-CT slices [μm]	–	3.6		2.5	2.3		–
	Lamellar thickness estimated from color mapping [μm]	–		6.9		4.2		–
Sample B	**Property**	**EV1**	**LV1**	**LV2**	**LV3**	**H-L**	**LV4**	**EV2**
B2 Magenta	Lamella angle (to Y axis) [°]	–	25	28	34	28	17	–
	Lamellar thickness estimated from nano-CT slices [μm]	–	2.0	3.2	2.3	–	1.9	–
	Lamellar thickness estimated from color mapping [μm]	–	2.5	3.2	2.0	–	3.0	–

patterns is also possible and was observed by Varga et al. [38] and Schrof et al. [94]. within neighboring bone regions (<100 μm). Following the rather broad angle value distribution in Fig. 5I and F-G, the LV1 layer supposedly includes an overlap region between two lamellae or a disordered interlamellar zone. According to the light microscopy images (Fig. 1), this layer may contain an interface between two interstitial zones, hence including a disordered region.

We have observed visible changes in MCF orientation in sample B2 Magenta (Fig. 6) as well, as seen in the slice through and MCF segmentation in Video SV5, Supporting Information. However, the supposed lamellar division shown in Fig. 6A appeared less regular compared to the abovementioned samples, with an inclination angle of lamellar layers changing from 34° to 17° with the insertion of a half-layer (H-L). This sample shows the best match between two methods of studying lamellar arrangement with all layers from nano-CT slices segmentation (Fig. 6A) being directly reflected by orientation color mapping (Fig. 6B). Unfortunately, due to lamellar structure complexity, we could not perform a new LV-specific MCF orientation segmentation and calculate MCF angle variations similar to the aforementioned samples.

We did not observe significant variations in the density of segmented MCFs between the lamellae within the examined nano-CT volumes (Table S4, Supporting Information), opposing to the model supported by Marroti [35] and observations of Reznikov et al. [22,82]. However, this might be due to the character of our manual segmentation of lamellar borders, where some of the proposed lamellar layers may include or in their entirety may be composed of disordered regions. The thickness of the measured lamellae varied from 2.3 μm to 4.5 μm as seen from the nano-CT slices and from 2.0 μm to 6.9 μm as hinted by MCF orientation distribution; these values are consistent with earlier reported results [22, 34,35]. Moreover, we only examined the inferomedial site of the femoral neck, thus the observed bone ultrastructure might be a result of life-long exposure to the compressive loads [95]. While the extracted sample volumes were predominantly co-aligned with the main axis of the femoral neck, their precise orientation is impeded by macroscale variations in femur morphology. It is of high interest to expand the number of investigated volumes and different skeleton sites in potential follow-up studies.

Knowing the geometry of bone lamellae, it is interesting to explore their mutual orientation with the LCN. Fig. 6d-G renders chosen LV to reflect their interaction with canaliculi. For the osteonal tissue in A4 Cyan, the canaliculi are running roughly orthogonal to the lamellae and seem to slowly converge in the direction of LV1 (Fig. 6D), most likely to a lacuna outside of the imaged volume. In the interstitial tissue A3 Green and B2 Magenta the structural co-localization of LCN and lamellae appears more complex. The majority of canaliculi still run orthogonally, for example those penetrating LV1 in B2 Magenta (Fig. 6E) or LV2 in A3 Green (Fig. 6F). At the same time, the thick canaliculus propagating between EV1 and LV2 in A3 Green, as well as lots of branches in both samples follow a different direction. Fig. 6F shows thin discontinuous channels running parallel to the lamellar boundary of LV3 and LV2 layer in A3 Green. Notably, it is also the region where the abovementioned switch in MCF orientation between LV2 and LV3 occurs. In B2 Magenta most branching occurs in the space between LV1 and LV3 volumes (Fig. 6E), where the MCF direction is closer to horizontal (orthogonal to the femoral neck axis). Notably, the insertion of a half-layer between LV3 and LV4 also seems to start at a canaliculus, running parallel to the lamellae (see dashed circles in Fig. 6A, E and joined 3D render in Video SV5, Supporting Information). The appearance of LCN units thus seems to be connected to the changes in lamellar structure [96,97], however the exact relationship is not apparent. The local MCF orientation analysis in the vicinity of the canaliculi and exploration of other structures related to ion transport, such as the recently reported cortical nanochannel network [98], fell below the resolution limit of the nano-CT setup. High-resolution methods like electron tomography would be more applicable for such tasks in the future [45,99].

3.4. MCF orientation correlative analyses

The spatial orientation of the mineralized collagen fibrils was assessed and compared between both techniques: nano-CT and qPRS. The latter method based on polarized Raman spectroscopy gives indirect information about the orientation of the MCFs, as estimated from the polarization-dependence of the ratio of amide I/amide III Raman band integral areas, following careful calibration of the setup on mineralized turkey leg tendon as model material [51,100]. MCF orientation was then mapped over the cortical bone area of interest, approximately 5 μm underneath the sample top surface. Due to focal spot size of the Raman spectrometer, each analyzed point represents a volume of ~(1 μm)^3, from which the mean local orientation of the MCFs was estimated. This data was compared to the estimated MCF orientation from segmented mineral ellipsoids in nano-CT scans.

For the correlative analysis of the MCFs angles, both measurements were transformed into the right-hand Tait-Bryan angle notation [67], where in-plane rotation (relative to the plane of qPRS measurement) is characterized by angle $\psi \in [-\pi,\pi]$, and out-of-plane rotation is characterized by angle $\theta \in [0,/2]$. MCFs were considered as cylinders, possessing radial symmetry, thus the rotation (φ) around the main MCFs axis was irrelevant for our measurement. The intersecting locations of both measurements were found by selecting the MCFs segments from the nano-CT scans fully or partially located in the extended volumes of qPRS measurement (see Materials and Methods section 2.4 and Supplementary chapter S5, Supporting Information). We chose a larger accepting volume (2 × 2 × 2 μm per measurement point), to increase the minimum number of ellipsoid segments contained within the intercepting volume for better statistical representation. For each point of qPRS measurement map, the averaged orientation of the matching MCFs segments in the nano-CT reconstructions (n = 2-29 per point, see Table S7, Supporting

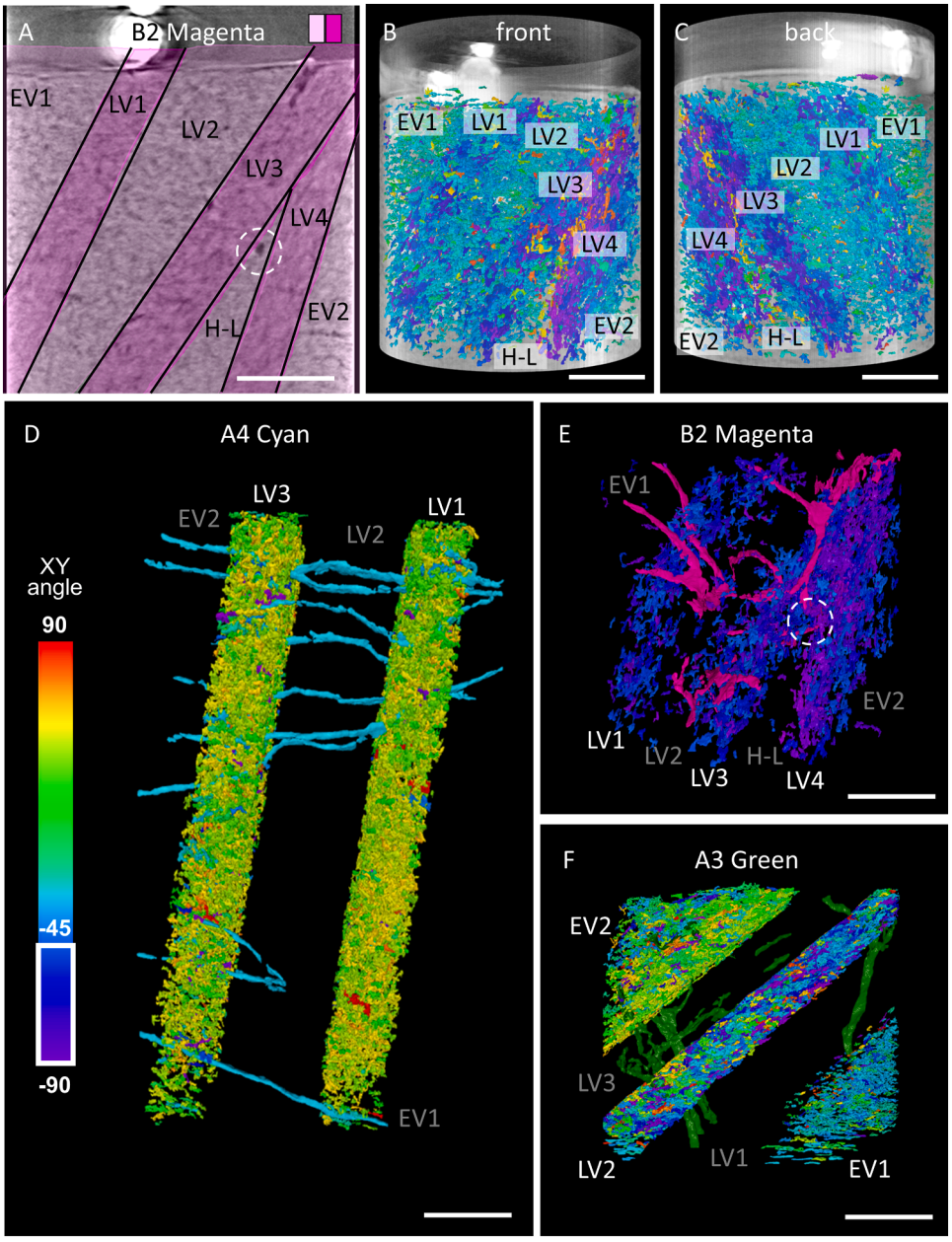

Fig. 6. Relative orientation of bone lamellae and LCN: (A) - lamellar structure identified following Video SV5 for B2 Magenta, (B, C) - 3D views showing segment orientation throughout the nano-CT volume. (D, E, F) – joined 3D renders of LCN and MCF orientation segmentation in A4 Cyan, B2 Magenta and A3 Green, respectively. (D) features a common color scale reflecting segment orientation in XY plane (see Fig. 5D). In (D) and (C), intermediate LV are omitted to simplify the view of LCN; in (B), since no individual sub-volumes were segmented, only the segments of angle values below −45° are displayed, being the main constituents of LV 1,3 and 4. Dashed circles in (A) and (E) indicate a canaliculus at the origin of H-L. Scale bars are 5 μm.

Information) was extracted and compared to the qPRS data. Fig. 7 reveals the positions of intersecting sites and compares the qPRS composition analysis and nano-CT lamellation study for sample A3 Green. Overlays of measurement sites for other samples, together with qPRS point numbering scheme can be seen in Figure S6, Supporting Information. Overlays of the qPRS measurement outputs (out-of-plane angle, mineral/matrix ratio, amide I sub-bands ratio) over the pillars top can be found in Figure S6, Supporting Information.

Point-by-point polar maps comparing in-plane ψ and out-of-plane θ angle values between both methods for each singular measurement point in A-series samples are plotted in Figure S9, Supporting Information. For the majority of measurement sites, both ψ and θ angle measurements between two techniques appear to correlate. Because the qPRS method was, strictly speaking, only calibrated for the out-of-plane θ angles of the MCFs [51], we further discuss only that parameter. The summarized comparison of the out-of-plane MCFs angles θ estimated from the qPRS and nano-CT methods across all samples and datapoints is shown in Fig. 8. Depicted angular errors for nano-CT represent the individual standard deviations of the segment orientations, while the error from the qPRS method for all points was equal to 9.7°, which is the error from the calibration function [51]. The collected angular values concentrate in the 15° - 60° range, with the largest number of values for the B2 Magenta sample, where a dense qPRS map was collected (81 vs. 25 points as for other samples). The correlation efficiency between the two techniques was estimated as the root means square error (RMSE) in relation to 1–1 line. The B2 Magenta sample exhibited generally higher RMSE values of 13.8°, when compared the 12.9° for the remaining samples. In particular, angular values for B2 Magenta are consistently

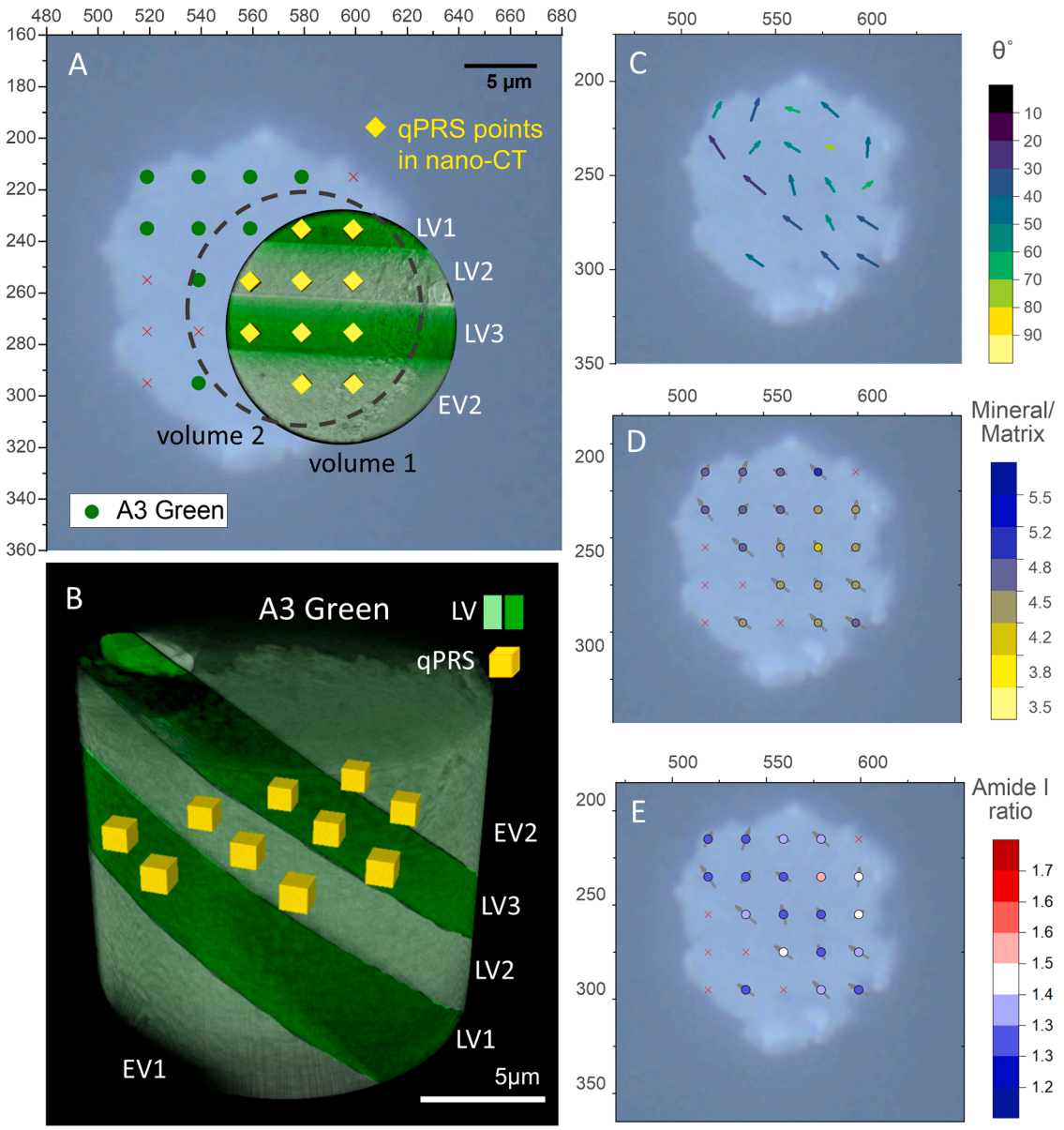

Fig. 7. Example of site-matched nanoCT+qPRS measurements within the A3 Green volume: Raman measurement points (A) and the respective composition maps (C-E) are shown in the context of imaged nano-CT volumes and derived lamellation pattern in the light microscopy top-view image (A) and in the 3D rendering of the lamella-segmented nano-CT volume (B). In (A,B), the cubes representing coinciding volumes, have a wall size of 1 µm. In (C), the estimated MCF orientation is shown with arrows; the length and the color of the arrows represent the out-of-plane MCF angle (90° matches the femoral neck main axis), while the arrow direction matches the in-plane MCF orientation. (D) and (E) is the mineral to matrix ratio and the Amide I sub-band ratio (lower values (blue) indicate a higher ordering) respectively (cf. Fig. 4).

over-/underestimated between qPRS and nano-CT techniques, indicating a possible influence of the sample inclination differences between the measurements. Nevertheless, the collective sample RMSE = 13.5° was close to the error of the qPRS method (9.7°) [51].

3.5. Methodological insights and limitations

Site-matched qPRS and nano-CT offer complementary insights on bone structural organization at sub-lamellar resolution. Raman spectroscopy is, however, limited by the sample turbidity [101], providing mostly 2D data on the MCF orientation in contrast to 3D analysis from nano-CT scans. Moreover, the different operating principles of the techniques yield different spatial resolution: ~50 nm for nano-CT vs. ~1 µm spot size for qPRS. At the same time, Raman spectroscopy enables to scan larger areas in a shorter time, while providing both structural and compositional information. However, qPRS mapping seems to be failing to detect interlamellar regions due to the low SNR from MCF collagen bands. In that regard, nano-CT is better suited to the lamellation pattern analysis, providing volumetric data on MCFs orientation. Phase-contrast nano-CT proved an excellent tool for imaging native unstained bone material, capable of resolving individual mineral ellipsoids while providing a vast amount of data for their quantification and a good overview of LCN and lamella boundaries.

It is important to keep in mind that nano-CT measurements give only an indirect estimation of the MCF orientation through the long axis of mineral ellipsoids. The latter is generally accepted to be co-aligned with the main axis of the MCF as concluded from earlier studies [78,79]. Here, we moreover confirm the co-alignment of the MCF with the segmented mineral ellipsoids via the qPRS technique. qPRS was previously calibrated and validated on a model material with the gold

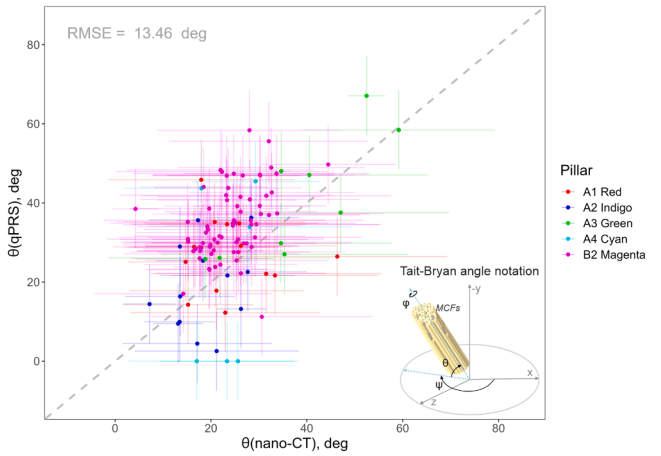

Fig. 8. Correlative analysis for the out-of-plane MCFs angle (θ) as assessed by qPRS and nano-CT segmentation with marked standard deviations for each measurement point. Schematic MCFs orientation is depicted in the Tait-Bryan angle notation with the Y-axis pointing opposite to femoral neck direction (Fig. 1 arrow).

standard SAXS method for MCF orientation estimation [51]. However, it would also be interesting to further validate the co-orientation of the mineral ellipsoids detected with the nano-CT with the true MCF orientation via ultra-high-resolution modalities like electron tomography and atom probe tomography.

Given the structural heterogeneity of bone, it is crucial to place the sampled small volumes into the proper biological contest [5]. Herein-described utilization of nano-CT could benefit from a combination with a large field-of-view technique such as confocal scanning laser microscopy or third harmonic generation microscopy to provide 3D context of lacunae and osteonal division [102]. The nano-CT instrument used in this study possesses, apart from the applied high-resolution (HRES) mode, a second large-field-of-view (LFOV) mode with 64 μm x 64 μm field of view at 150 nm nominal resolution. Future studies applying scale-bridging nano-CT (by first cutting larger pillars for LFOV and subsequently milling them down for HRES) are very promising, as that would allow positioning high-resolution volumes with respect to lacunae and trace orientation changes throughout multiple adjacent lamellae. Laser ablation was extremely helpful in isolating bone volumes for nano-CT imaging to improve SNR and avoid interior tomography artifacts. On the downside, it has introduced surface damage of about 1.5–2.5 μm to the utmost edge of fabricated pillars that compromised and impeded the identification and analysis of bone-building blocks in this zone. Alternative to the laser ablation, micro-lathe milling of cylindrical samples can be utilized for a high-throughput sample preparation [103]. The inclusion of sample surface markup grids via laser ablation is another promising approach to facilitate sample navigation and orientation when correlating numerous methods for bone ultrastructure characterization [104]. With these remarks in mind, the measurement approach using nano-CT described in this study has a high potential in further analysis of the bone ultrastructure in laboratory settings.

This study would not have been possible without advanced 3D data treatment tools. Transformation operations of the slicing plane were imperative to discover the lamellar arrangement. Machine learning segmentation of mineral ellipsoids became the backbone for their orientation study, providing a more feature-specific alternative to Fourier transform [36] or greyscale gradient tensor [105]-based approaches, and allowing subsequent morphological analysis. Improving on these tools and enhancing the feature segmentation with machine learning algorithms, including deep learning schemes [106,107], will allow for more efficient use of 3D data and better representation of studied objects. Quantitative orientation studies in 3D space using 3D analysis software could be eased by adding customizability to coordinate system choices as well as direct export of rotation matrices or open scripting.

This work utilized a bone sample from a single donor and anatomical site. While this approach was appropriate for the current exploratory study, future research would benefit from a larger, more diverse sample to examine variations across different anatomical sites and disease conditions.

4. Conclusion

This exploratory study highlights important details on the lamellar and sub-lamellar bone organization, namely zonal variations between osteonal and interstitial types, LCN structure, MCF arrangement and lamellar organization. Sample preparation method based on femtosecond-laser ablation allowed pinpointing volumes of interest, and improving quality of collected tomography data. Imaging capabilities of laboratory-based Zernike phase-contrast nano-CT together with employed machine learning segmentation algorithms, enabled visualization of MCF organization at a high spatial resolution. Performing site-matched nano-CT and qPRS allowed us to combine structural and compositional datasets. The measured MCF out-of-plane angles were in good agreement between the two methods (13.5° RMSE), approaching the resolution limit of qPRS (~9.7°).

Data treatment strategies and correlative experiment workflows described here could be adapted to other fields concerning ordered hierarchical materials of similar feature size, such as cellulose- and chitin-based nature-derived materials as well as man-made filler-enhanced composites and architected materials. In future studies of human bone ultrastructure, including more patients and VOIs should allow a statistically sound analysis of trends and differences presented in the current work. Furthermore, other bone ultrastructural units of interest like interlamellar and cement interfaces could be focused on, and the structure of MCF around lacunae and near Haversian channels could be studied in more detail. Moreover, the influence of bone metabolic diseases on the bone ultrastructure could be investigated.

Funding

This work was supported by the Special Focus Area Personalized Health and Related Technologies (SFA PHRT) iDoc Project 2017-304. We acknowledge funding by the Deutsche Forschungsgemeinschaft (DFG, German Research Foundation) - Project-ID 416229255 - SFB 1411.

Ethical approval

This study was conducted in accordance with the principles of the Helsinki Declaration. All experiments were performed in accordance with the guidelines and regulations of the Ethics Committee for Research on Humans of the Canton Bern, Switzerland (NO. 2018-01815).

Data availability statement

Original data including raw nano-CT tilt series, SIRT reconstruction slices, individual Raman spectra and light microscopy images is publicly available on Zenodo: Kormilina, T., & Kochetkova, T. (2024). Human Bone Ultrastructure in 3D (nano-CT+qPRS): Data Archive. Zenodo. https://zenodo.org/doi/10.5281/zenodo.11422941.

CRediT authorship contribution statement

Tatiana Kochetkova: Writing – review & editing, Writing – original draft, Visualization, Validation, Project administration, Methodology, Investigation, Formal analysis, Data curation, Conceptualization. **Tatiana Kormilina:** Writing – review & editing, Writing – original draft,

Visualization, Validation, Software, Project administration, Methodology, Investigation, Formal analysis, Data curation, Conceptualization. **Silvan Englisch:** Writing – review & editing, Supervision, Methodology, Investigation, Formal analysis, Conceptualization. **Dominik Drobek:** Writing – review & editing, Supervision, Software, Methodology. **Benjamin Apeleo Zubiri:** Writing – review & editing, Supervision, Project administration, Methodology, Investigation, Conceptualization. **Oliver Braun:** Writing – review & editing, Software, Methodology, Investigation. **Michel Calame:** Writing – review & editing, Supervision, Project administration. **Stefan Remund:** Writing – review & editing, Methodology, Investigation. **Beat Neuenschwander:** Writing – review & editing, Supervision, Methodology. **Johann Michler:** Writing – review & editing, Supervision, Resources. **Philippe Zysset:** Writing – review & editing, Supervision, Resources, Project administration. **Erdmann Spiecker:** Writing – review & editing, Supervision, Resources, Project administration, Funding acquisition, Conceptualization. **Jakob Schwiedrzik:** Writing – review & editing, Supervision, Resources, Project administration, Funding acquisition, Conceptualization.

Declaration of competing interest

The authors declare that they have no known competing financial interests or personal relationships that could have appeared to influence the work reported in this paper.

Acknowledgements

The authors would like to thank Taras Puchka for his help developing the angle correlation scripts, Janis Wirth for sharing his knowledge of nano-CT operation and 3D data analysis, Rico Muff for his support during qPRS measurements, Lilian Vogl & Peter Schweizer for sample transport in COVID pandemic conditions. We thank the Center of Advanced Materials and Processes (ZMP) in Fürth, Germany for letting us use their equipment for control Raman measurements between nano-CT runs and Alexander Götz for helping us make original nano-CT data available for public.

Supplementary materials

Supplementary material associated with this article can be found, in the online version, at doi:10.1016/j.actbio.2025.03.045.

References

[1] P. Fratzl, R. Weinkamer, Nature's hierarchical materials, Prog. Mater. Sci. 52 (2007) 1263–1334, https://doi.org/10.1016/j.pmatsci.2007.06.001.
[2] M. Eder, S. Amini, P. Fratzl, Biological composites-complex structures for functional diversity, n.d. https://www.science.org.
[3] N. Reznikov, J.A.M. Steele, P. Fratzl, M.M. Stevens, A materials science vision of extracellular matrix mineralization, Nat. Rev. Mater. 1 (2016), https://doi.org/10.1038/natrevmats.2016.41.
[4] Z. Liu, Z. Zhang, R.O. Ritchie, Structural orientation and anisotropy in biological materials: functional designs and mechanics, Adv. Funct. Mater. 30 (2020), https://doi.org/10.1002/adfm.201908121.
[5] A. Rodriguez-Palomo, M. Østergaard, H. Birkedal, Bone hierarchical structure: heterogeneity and uniformity, Adv. Funct. Mater. (2023), https://doi.org/10.1002/adfm.202307026.
[6] J.D. Currey, Bones: Structure and Mechanics, 2013.
[7] A.L. Boskey, Bone composition: relationship to bone fragility and antiosteoporotic drug effects, Bonekey. Rep. 2 (2013), https://doi.org/10.1038/bonekey.2013.181.
[8] S. Bracher, B. Voumard, M. Simon, T. Kochetkova, M. Pretterklieber, P. Zysset, Bone collagen tensile properties of the aging human proximal femur, Bone Rep. 21 (2024), https://doi.org/10.1016/j.bonr.2024.101773.
[9] E.A. Zimmermann, R.O. Ritchie, Bone as a structural material, Adv. Healthc. Mater. 4 (2015) 1287–1304, https://doi.org/10.1002/adhm.201500070.
[10] S. Jia, T. Tao, J. Sun, J. Du, Y. Xie, L. Yu, W. Tang, J. Wang, J. Gong, Understanding hierarchical structure construction strategies and biomimetic design principles: a review, Small. Struct. 4 (2023), https://doi.org/10.1002/sstr.202300139.
[11] S. Kim, C.B. Park, Bio-inspired synthesis of minerals for energy, environment, and medicinal applications, Adv. Funct. Mater. 23 (2013) 10–25, https://doi.org/10.1002/adfm.201201994.
[12] X. Wei, J. Chen, H.Y. Shen, K. Jiang, H. Ren, Y. Liu, E. Luo, J. Zhang, J.Z. Xu, Z. M. Li, Hierarchically biomimetic scaffolds with anisotropic micropores and nanotopological patterns to promote bone regeneration via geometric modulation, Adv. Healthc. Mater. (2024), https://doi.org/10.1002/adhm.202304178.
[13] X. Shi, F. Wang, B.G. Lougou, H. Zhang, X. Wei, D. Li, J. Xu, Experimental and numerical study regarding the biomimetic bone porous structure to match energy and mass flow in a solar thermochemical reactor, J. Energy Storage 55 (2022), https://doi.org/10.1016/j.est.2022.105645.
[14] A. Nouri, A. Zarkesh, Efficient configuration in architectural structures based on biomimicry principles in femur bone using hurricane geometry, Innov. Infrastruct. Sol. 9 (2024), https://doi.org/10.1007/s41062-023-01348-7.
[15] P. Augat, S. Schorlemmer, The role of cortical bone and its microstructure in bone strength, Age Ageing 35 (2006) 27–31, https://doi.org/10.1093/ageing/afl081.
[16] J. Jowsey, Studies of Haversian systems in man and some animals, J. Anat. 100 (1966) 857–864.
[17] K. Raum, I. Leguerney, F. Chandelier, M. Talmant, A. Saïed, F. Peyrin, P. Laugier, Site-matched assessment of structural and tissue properties of cortical bone using scanning acoustic microscopy and synchrotron radiation μct, Phys. Med. Biol. 51 (2006) 733–746, https://doi.org/10.1088/0031-9155/51/3/017.
[18] N.K. Wittig, J. Palle, M. Østergaard, S. Frølich, M.E. Birkbak, K.M. Spiers, J. Garrevoet, H. Birkedal, Bone biomineral properties vary across Human osteonal Bone, ACS Nano 13 (2019) 12949–12956. https://doi.org/10.1021/acsnano.9b05535.
[19] I. Jimenez-Palomar, A. Shipov, R. Shahar, A.H. Barber, Structural orientation dependent sub-lamellar bone mechanics, J. Mech. Behav. Biomed. Mater. 52 (2015) 63–71, https://doi.org/10.1016/j.jmbbm.2015.02.031.
[20] M. Georgiadis, R. Müller, P. Schneider, Techniques to assess bone ultrastructure organization: orientation and arrangement of mineralized collagen fibrils, J. R. Soc. Interface 13 (2016), https://doi.org/10.1098/rsif.2016.0088.
[21] M. Unal, O. Akkus, Raman spectral classification of mineral- and collagen-bound water's associations to elastic and post-yield mechanical properties of cortical bone, Bone 81 (2015) 315–326, https://doi.org/10.1016/j.bone.2015.07.024.
[22] N. Reznikov, R. Shahar, S. Weiner, Three-dimensional structure of human lamellar bone: the presence of two different materials and new insights into the hierarchical organization, Bone 59 (2014) 93–104, https://doi.org/10.1016/j.bone.2013.10.023.
[23] W. Gebhardt, Über Funktionell Wichtige Anordnungsweisen der Feineren und Gröberen Bauelemente des Wirbeltierknochens, 1905.
[24] A. Ascenzi, E. Bonucci, The tensile properties of single osteons, Anat. Rec. 158 (1967) 375–386, https://doi.org/10.1002/ar.1091580403.
[25] A. Ascenzi, E. Bonucci, P. Generali, A. Ripamonti, N. Roverf, Orientation of apatite in single osteon samples as studied by pole figures, Calcif. Tiss. Int. 29 (1979) 101–105.
[26] A. Ascenzi, E. Bonucci, A. Ripamonti, N. Roveri, X-ray diffraction and electron microscope study of osteons during calcification, Calcif. Tiss. Res 25 (1978) 133–143.
[27] S. Weiner, W. Traub, H.D. Wagner, Lamellar bone: structure–function relations, J. Struct. Biol. 126 (1999) 241–255, https://doi.org/10.1006/JSBI.1999.4107.
[28] J.Y. Rho, T.Y. Tsui, G.M. Pharr, Elastic properties of human cortical and trabecular lamellar bone measured by nanoindentation, Biomaterials 18 (1997) 1325–1330, https://doi.org/10.1016/S0142-9612(97)00073-2.
[29] G. Franzoso, P.K. Zysset, Elastic anisotropy of human cortical bone secondary osteons measured by nanoindentation, J. Biomech. Eng. 131 (2009) 1–11, https://doi.org/10.1115/1.3005162.
[30] N. Reznikov, R. Shahar, S. Weiner, Bone hierarchical structure in three dimensions, Acta Biomater. 10 (2014) 3815–3826, https://doi.org/10.1016/j.actbio.2014.05.024.
[31] T.G. Bromage, H.M. Goldman, S.C. McFarlin, J. Warshaw, A. Boyde, C.M. Riggs, Circularly polarized light standards for investigations of collagen fiber orientation in bone, Anat. Rec. B 274 (2003) 157–168, https://doi.org/10.1002/ar.b.10031.
[32] A.G. Reisinger, D.H. Pahr, P.K. Zysset, Elastic anisotropy of bone lamellae as a function of fibril orientation pattern, Biomech. Model. Mechanobiol. 10 (2011) 67–77, https://doi.org/10.1007/s10237-010-0218-6.
[33] S. Weiner, W. Traub, H.D. Wagner, Lamellar bone: structure–Function relations, J. Struct. Biol. 126 (1999) 241–255, https://doi.org/10.1006/JSBI.1999.4107.
[34] W. Wagermaier, H.S. Gupta, A. Gourrier, M. Burghammer, P. Roschger, P. Fratzl, Spiral twisting of fiber orientation inside bone lamellae, Biointerphases 1 (2006) 1–5, https://doi.org/10.1116/1.2178386.
[35] G. Marotti, A New Theory of Bone Lamellation, 1993.
[36] E. Raguin, K. Rechav, R. Shahar, S. Weiner, Focused ion beam-SEM 3D analysis of mineralized osteonal bone: lamellae and cement sheath structures, Acta Biomater. 121 (2021) 497–513, https://doi.org/10.1016/j.actbio.2020.11.002.
[37] M. Langer, A. Pacureanu, H. Suhonen, Q. Grimal, P. Cloetens, F. Peyrin, X-ray phase nanotomography resolves the 3D Human bone ultrastructure, PLoS ONE 7 (2012) e35691, https://doi.org/10.1371/JOURNAL.PONE.0035691.
[38] P. Varga, A. Pacureanu, M. Langer, H. Suhonen, B. Hesse, Q. Grimal, P. Cloetens, K. Raum, F. Peyrin, Investigation of the three-dimensional orientation of mineralized collagen fibrils in human lamellar bone using synchrotron X-ray phase nano-tomography, Acta Biomater. 9 (2013) 8118–8127, https://doi.org/10.1016/j.actbio.2013.05.015.

[39] M. Dierolf, A. Menzel, P. Thibault, P. Schneider, C.M. Kewish, R. Wepf, O. Bunk, F. Pfeiffer, Ptychographic X-ray computed tomography at the nanoscale, Nature 467 (2010) 436–439, https://doi.org/10.1038/nature09419.
[40] A. Ciani, H. Toumi, S. Pallu, E.H.R. Tsai, A. Diaz, M. Guizar-Sicairos, M. Holler, E. Lespessailles, C.M. Kewish, Ptychographic X-ray CT characterization of the osteocyte lacuno-canalicular network in a male rat's glucocorticoid induced osteoporosis model, Bone Rep. 9 (2018) 122–131, https://doi.org/10.1016/j.bonr.2018.07.005.
[41] M. Liebi, M. Georgiadis, A. Menzel, P. Schneider, J. Kohlbrecher, O. Bunk, M. Guizar-Sicairos, Nanostructure surveys of macroscopic specimens by small-angle scattering tensor tomography, Nature 527 (2015) 349–352, https://doi.org/10.1038/nature16056.
[42] T.A. Grünewald, M. Liebi, N.K. Wittig, A. Johannes, T. Sikjaer, L. Rejnmark, Z. Gao, M. Rosenthal, M. Guizar-Sicairos, H. Birkedal, M. Burghammer, Mapping the 3D orientation of nanocrystals and nanostructures in human bone: indications of novel structural features, Sci. Adv. 6 (2020) 4171–4183, https://doi.org/10.1126/SCIADV.ABA4171/SUPPL_FILE/ABA4171_SM.PDF.
[43] T.A. Grünewald, A. Johannes, N.K. Wittig, J. Palle, A. Rack, M. Burghammer, H. Birkedal, Bone mineral properties and 3D orientation of human lamellar bone around cement lines and the haversian system, IUCrJ. 10 (2023) 189–198, https://doi.org/10.1107/S2052252523000866.
[44] P. Schneider, M. Meier, R. Wepf, R. Müller, Serial FIB/SEM imaging for quantitative 3D assessment of the osteocyte lacuno-canalicular network, Bone 49 (2011) 304–311, https://doi.org/10.1016/j.bone.2011.04.005.
[45] C. Micheletti, F.A. Shah, A. Palmquist, K. Grandfield, Ultrastructure and nanoporosity of Human bone shown with correlative on-axis electron and spectroscopic tomographies, ACS Nano 17 (2023) 24710–24724, https://doi.org/10.1021/acsnano.3c04633.
[46] E. McNally, F. Nan, G.A. Botton, H.P. Schwarcz, Scanning transmission electron microscopic tomography of cortical bone using Z-contrast imaging, Micron. 49 (2013) 46–53, https://doi.org/10.1016/j.micron.2013.03.002.
[47] N. Reznikov, M. Bilton, L. Lari, M.M. Stevens, R. Kröger, Fractal-like hierarchical organization of bone begins at the nanoscale, Science (2018) 360, https://doi.org/10.1126/science.aao2189.
[48] B.E.J. Lee, B. Langelier, K. Grandfield, Visualization of collagen–Mineral arrangement using atom probe tomography, Adv. Biol. 5 (2021), https://doi.org/10.1002/adbi.202100657.
[49] H.D. Barth, E.A. Zimmermann, E. Schaible, S.Y. Tang, T. Alliston, R.O. Ritchie, Characterization of the effects of x-ray irradiation on the hierarchical structure and mechanical properties of human cortical bone, Biomaterials 32 (2011) 8892–8904, https://doi.org/10.1016/j.biomaterials.2011.08.013.
[50] X. Lu, M.P. Fernández, R.S. Bradley, S.D. Rawson, M. O'Brien, B. Hornberger, M. Leibowitz, G. Tozzi, P.J. Withers, Anisotropic crack propagation and deformation in dentin observed by four-dimensional X-ray nano-computed tomography, Acta Biomater. 96 (2019) 400–411, https://doi.org/10.1016/j.actbio.2019.06.042.
[51] T. Kochetkova, C. Peruzzi, O. Braun, J. Overbeck, A.K. Maurya, A. Neels, M. Calame, J. Michler, P. Zysset, J. Schwiedrzik, Combining polarized Raman spectroscopy and micropillar compression to study microscale structure-property relationships in mineralized tissues, Acta Biomater. 119 (2021) 390–404, https://doi.org/10.1016/j.actbio.2020.10.034.
[52] F. Nicolson, M.F. Kircher, N. Stone, P. Matousek, Spatially offset Raman spectroscopy for biomedical applications, Chem. Soc. Rev. 50 (2021) 556–568, https://doi.org/10.1039/d0cs00855a.
[53] F.W.L. Esmonde-White, M.D. Morris, Validating in vivo Raman spectroscopy of bone in human subjects, 8565 (2013) 810–816. https://doi.org/10.1117/12.2005679.
[54] T. Kormilina, S. Englisch, T. Kochetkova, D. Drobek, J. Wirth, B.A. Zubiri, J. Schwiedrzik, E. Spiecker, Multi-modal characterization of collagen fibril orientation in human cortical bone by a combination of quantitative polarized Raman spectroscopy, nanoscale X-ray computed tomography and 360° electron tomography, Microsc. Microanal. 27 (2021) 96–101, https://doi.org/10.1017/s1431927621000970.
[55] T. Kochetkova, M.S. Hanke, M. Indermaur, A. Groetsch, S. Remund, B. Neuenschwander, J. Michler, K.A. Siebenrock, P. Zysset, J. Schwiedrzik, Composition and micromechanical properties of the femoral neck compact bone in relation to patient age, sex and hip fracture occurrence, Bone 177 (2023), https://doi.org/10.1016/j.bone.2023.116920.
[56] T. Kochetkova, A. Groetsch, M. Indermaur, C. Peruzzi, S. Remund, B. Neuenschwander, B. Bellon, J. Michler, P. Zysset, J. Schwiedrzik, Assessing minipig compact jawbone quality at the microscale, J. Mech. Behav. Biomed. Mater. 134 (2022) 105405, https://doi.org/10.1016/j.jmbbm.2022.105405.
[57] F. Zernike, Phase contrast, a new method for the microscopic observation of transparent objects, Physica 9 (1942) 686–698, https://doi.org/10.1016/S0031-8914(42)80035-X.
[58] F. Zernike, Phase contrast, a new method for the microscopic observation of transparent objects part II, Physica 9 (1942) 974–986, https://doi.org/10.1016/S0031-8914(42)80079-8.
[59] J. Wang, Y. Karen Chen, Q. Yuan, A. Tkachuk, C. Erdonmez, B. Hornberger, M. Feser, Automated markerless full field hard x-ray microscopic tomography at sub-50 nm 3-dimension spatial resolution, Appl. Phys. Lett. 100 (2012), https://doi.org/10.1063/1.3701579.
[60] W. van Aarle, W.J. Palenstijn, J. De Beenhouwer, T. Altantzis, S. Bals, K. J. Batenburg, J. Sijbers, The ASTRA Toolbox: a platform for advanced algorithm development in electron tomography, Ultramicroscopy 157 (2015) 35–47, https://doi.org/10.1016/J.ULTRAMIC.2015.05.002.
[61] C. Sommer, C. Straehle, U. Kothe, F.A. Hamprecht, Ilastik: interactive learning and segmentation toolkit, in: Proceedings - International Symposium on Biomedical Imaging, 2011, pp. 230–233, https://doi.org/10.1109/ISBI.2011.5872394.
[62] A.J. Makowski, C.A. Patil, A. Mahadevan-Jansen, J.S. Nyman, Polarization control of Raman spectroscopy optimizes the assessment of bone tissue, J. Biomed. Opt. 18 (2013), https://doi.org/10.1117/1.JBO.18.5.
[63] M. Unal, S. Uppuganti, S. Timur, A. Mahadevan-Jansen, O. Akkus, J.S. Nyman, Assessing matrix quality by Raman spectroscopy helps predict fracture toughness of human cortical bone, Sci. Rep. 9 (2019) 1–13, https://doi.org/10.1038/s41598-019-43542-7.
[64] M. Unal, H. Jung, O. Akkus, Novel Raman spectroscopic biomarkers indicate that postyield damage denatures bone's collagen, J. Bone Mineral Res. 31 (2016) 1015–1025, https://doi.org/10.1002/jbmr.2768.
[65] G. Van Rossum, F.L. Drake, Python 3 Reference Manual, CreateSpace., Scotts Valley, CA, 2009.
[66] T. Kormilina, T. Kochetkova, Data archive: human bone ultrastructure in 3D (nano-CT+qPRS), (2024). 10.5281/zenodo.11422941.
[67] C.M. Roithmayr, D.H. Hodges, Dynamics: Theory and Application of Kane's Method,, 1st ed, Cambridge University Press, 2016.
[68] P. Berens, CircStat: a MATLAB toolbox for circular statistics, J. Stat. Softw. 31 (2009) 1–21, https://doi.org/10.18637/JSS.V031.I10.
[69] R Core Team, R: A Language and Environment for Statistical Computing, 2021.
[70] A. Kassambara, Practical Statistics in R for Comparing Groups: Numerical Variables, 1st ed., Datanovia.com, 2019.
[71] A. Zeileis, T. Hothorn, Diagnostic checking in regression relationships, R News 3 (2002) 7–10.
[72] N. Reznikov, M. Bilton, L. Lari, M.M. Stevens, R. Kröger, Fractal-like hierarchical organization of bone begins at the nanoscale, Science (2018) 360, https://doi.org/10.1126/SCIENCE.AAO2189/SUPPL_FILE/AAO2189S4.MP4.
[73] F.A. Shah, K. Ruscsák, A. Palmquist, Transformation of bone mineral morphology: from discrete marquise-shaped motifs to a continuous interwoven mesh, Bone Rep. 13 (2020) 100283, https://doi.org/10.1016/j.bonr.2020.100283.
[74] D.M. Binkley, J. Deering, H. Yuan, A. Gourrier, K. Grandfield, Ellipsoidal mesoscale mineralization pattern in human cortical bone revealed in 3D by plasma focused ion beam serial sectioning, J. Struct. Biol. 212 (2020), https://doi.org/10.1016/j.jsb.2020.107615.
[75] C. Micheletti, A. Hurley, A. Gourrier, A. Palmquist, T. Tang, F.A. Shah, K. Grandfield, Bone mineral organization at the mesoscale: a review of mineral ellipsoids in bone and at bone interfaces, Acta Biomater. 142 (2022) 1–13, https://doi.org/10.1016/j.actbio.2022.02.024.
[76] E. Macías-Sánchez, N.V. Tarakina, D. Ivanov, S. Blouin, A.M. Berzlanovich, P. Fratzl, Spherulitic crystal growth drives mineral deposition patterns in collagen-based materials, Adv. Funct. Mater. 32 (2022) 2200504, https://doi.org/10.1002/ADFM.202200504.
[77] D.J. Buss, N. Reznikov, M.D. McKee, Crossfibrillar mineral tessellation in normal and hyp mouse bone as revealed by 3D FIB-SEM microscopy, J. Struct. Biol. 212 (2020), https://doi.org/10.1016/j.jsb.2020.107603.
[78] P. Fratzl, H.S. Gupta, E.P. Paschalis, P. Roschger, Structure and mechanical quality of the collagen-mineral nano-composite in bone, J. Mater. Chem. 14 (2004) 2115–2123, https://doi.org/10.1039/b402005g.
[79] K. Grandfield, V. Vuong, Henry, P. Schwarcz, Ultrastructure of bone: hierarchical features from nanometer to micrometer scale revealed in focused ion beam sections in the TEM, Calcif. Tissue Int. 103 (2018) 606–616, https://doi.org/10.1007/s00223-018-0454-9.
[80] J.P.R.O. Orgel, T.C. Irving, A. Miller, T.J. Wess, Microfibrillar structure of type I collagen in situ, Proc. Natl. Acad. Sci. U. S. A. 103 (2006) 9001–9005, https://doi.org/10.1073/PNAS.0502718103/SUPPL_FILE/02718TABLE3.PDF.
[81] S. Englisch, J. Wirth, D. Drobek, B. Apeleo Zubiri, E. Spiecker, Expanding accessible 3D sample size in lab-based X-ray nanotomography without compromising resolution, Precis. Eng. 82 (2023) 169–183, https://doi.org/10.1016/j.precisioneng.2023.02.011.
[82] N. Reznikov, R. Almany-Magal, R. Shahar, S. Weiner, Three-dimensional imaging of collagen fibril organization in rat circumferential lamellar bone using a dual beam electron microscope reveals ordered and disordered sub-lamellar structures, Bone 52 (2013) 676–683, https://doi.org/10.1016/j.bone.2012.10.034.
[83] C.A. Schurman, S.W. Verbruggen, T. Alliston, Disrupted osteocyte connectivity and pericellular fluid flow in bone with aging and defective TGF-β signaling, Proc. Natl. Acad. Sci. U. S. A. 118 (2021) e2023999118, https://doi.org/10.1073/PNAS.2023999118/SUPPL_FILE/PNAS.2023999118.SM03.MOV.
[84] J. Chen, M. Aido, A. Roschger, A. van Tol, S. Checa, B.M. Willie, R. Weinkamer, Spatial variations in the osteocyte lacunocanalicular network density and analysis of the connectomic parameters, PLoS ONE 19 (2024), https://doi.org/10.1371/journal.pone.0303515.
[85] F. Repp, P. Kollmannsberger, A. Roschger, A. Berzlanovich, G.M. Gruber, P. Roschger, W. Wagermaier, R. Weinkamer, Coalignment of osteocyte canaliculi and collagen fibers in human osteonal bone, J. Struct. Biol. 199 (2017) 177–186, https://doi.org/10.1016/j.jsb.2017.07.004.
[86] E. Bortel, L.M. Grover, N. Eisenstein, C. Seim, H. Suhonen, A. Pacureanu, P. Westenberger, K. Raum, M. Langer, F. Peyrin, O. Addison, B. Hesse, Interconnectivity explains high canalicular network robustness between neighboring osteocyte lacunae in Human bone, Adv. Nanobiomed. Res. 2 (2022), https://doi.org/10.1002/anbr.202100090.
[87] N.K. Wittig, M. Laugesen, M.E. Birkbak, F.L. Bach-Gansmo, A. Pacureanu, S. Bruns, M.H. Wendelboe, A. Brüel, H.O. Sørensen, J.S. Thomsen, H. Birkedal,

Canalicular junctions in the osteocyte lacuno-canalicular network of cortical bone, ACS. Nano 13 (2019) 6421–6430, https://doi.org/10.1021/acsnano.8b08478.
[88] M.D. Morris, G.S. Mandair, Raman Assessment of Bone quality, Clin. Orthop. Relat. Res. 469 (2011) 2160–2169, https://doi.org/10.1007/s11999-010-1692-y.
[89] M. Unal, R. Ahmed, A. Mahadevan-Jansen, J.S. Nyman, Compositional assessment of bone by Raman spectroscopy, Analyst 146 (2021) 7444, https://doi.org/10.1039/d1an01560e.
[90] M.J. Mirzaali, J.J. Schwiedrzik, S. Thaiwichai, J.P. Best, J. Michler, P.K. Zysset, U. Wolfram, Mechanical properties of cortical bone and their relationships with age, gender, composition and microindentation properties in the elderly, Bone 93 (2016) 196–211, https://doi.org/10.1016/j.bone.2015.11.018.
[91] G.S. Mandair, M.D. Morris, Contributions of Raman spectroscopy to the understanding of bone strength, Bonekey. Rep. 4 (2015) 1–8, https://doi.org/10.1038/bonekey.2014.115.
[92] J.S. Nyman, A.J. Makowski, C.A. Patil, T.P. Masui, E.C. O'Quinn, X. Bi, S. A. Guelcher, D.P. Nicollela, A. Mahadevan-Jansen, Measuring differences in compositional properties of bone tissue by confocal Raman spectroscopy, Calcif. Tissue Int. 89 (2011) 111–122, https://doi.org/10.1007/s00223-011-9497-x.
[93] J. Burket, S. Gourion-Arsiquaud, L.M. Havill, S.P. Baker, A.L. Boskey, M.C.H. van der Meulen, Microstructure and nanomechanical properties in osteons relate to tissue and animal age, J. Biomech. 44 (2011) 277–284, https://doi.org/10.1016/j.jbiomech.2010.10.018.
[94] S. Schrof, P. Varga, L. Galvis, K. Raum, A. Masic, 3D Raman mapping of the collagen fibril orientation in human osteonal lamellae, J. Struct. Biol. 187 (2014) 266–275, https://doi.org/10.1016/j.jsb.2014.07.001.
[95] G. Grezzana, H.C. Loh, Z. Qin, M.J. Buehler, A. Masic, F. Libonati, Probing the role of bone lamellar patterns through collagen microarchitecture mapping, numerical modeling, and 3D-printing, Adv. Eng. Mater. 22 (2020), https://doi.org/10.1002/ADEM.202000387.
[96] M. Kerschnitzki, W. Wagermaier, P. Roschger, J. Seto, R. Shahar, G.N. Duda, S. Mundlos, P. Fratzl, The organization of the osteocyte network mirrors the extracellular matrix orientation in bone, J. Struct. Biol. 173 (2011) 303–311, https://doi.org/10.1016/j.jsb.2010.11.014.
[97] M. Kerschnitzki, P. Kollmannsberger, M. Burghammer, G.N. Duda, R. Weinkamer, W. Wagermaier, P. Fratzl, Architecture of the osteocyte network correlates with bone material quality, J. Bone Mineral Res. 28 (2013) 1837–1845, https://doi.org/10.1002/jbmr.1927.
[98] T. Tang, W. Landis, S. Blouin, L. Bertinetti, M.A. Hartmann, A. Berzlanovich, R. Weinkamer, W. Wagermaier, P. Fratzl, Subcanalicular nanochannel volume is inversely correlated with calcium content in Human cortical bone, J. Bone Mineral Res. 38 (2023) 313–325, https://doi.org/10.1002/jbmr.4753.
[99] K. Grandfield, C. Micheletti, J. Deering, G. Arcuri, T. Tang, B. Langelier, Atom probe tomography for biomaterials and biomineralization, Acta Biomater. 148 (2022) 44–60, https://doi.org/10.1016/j.actbio.2022.06.010.
[100] A.K. Maurya, A. Parrilli, T. Kochetkova, J. Schwiedrzik, A. Dommann, A. Neels, Multiscale and multimodal X-ray analysis: quantifying phase orientation and morphology of mineralized turkey leg tendons, Acta Biomater. 129 (2021) 169–177, https://doi.org/10.1016/j.actbio.2021.05.022.
[101] M. Raghavan, N.D. Sahar, R.H. Wilson, M.-A. Mycek, N. Pleshko, D.H. Kohn, M. D. Morris, Quantitative polarized Raman spectroscopy in highly turbid bone tissue, J. Biomed. Opt. 15 (2010) 037001, https://doi.org/10.1117/1.3426310.
[102] R. Genthial, E. Beaurepaire, M.C. Schanne-Klein, F. Peyrin, D. Farlay, C. Olivier, Y. Bala, G. Boivin, J.C. Vial, D. Débarre, A. Gourrier, Label-free imaging of bone multiscale porosity and interfaces using third-harmonic generation microscopy, Sci. Rep. 7 (2017) 1–16, https://doi.org/10.1038/s41598-017-03548-5.
[103] N.K. Wittig, C. Pedersen, J. Palle, M. Østergaard, T.E.K. Christensen, M. Kahnt, A. Sadetskaia, J.S. Thomsen, A. Brüel, H. Birkedal, Protocols for preparation of biomineralized samples for computed tomography, Tomogr. Mater. Struct. 5 (2024) 100027, https://doi.org/10.1016/j.tmater.2024.100027.
[104] T. Tang, T. Casagrande, P. Mohammadpour, W. Landis, B. Lievers, K. Grandfield, Characterization of human trabecular bone across multiple length scales: a correlative approach combining X-ray tomography with LaserFIB and plasma FIB-SEM, (2024). 10.21203/rs.3.rs-4254247/v1.
[105] S.P. Ojanen, M.A.J. Finnilä, W. Herzog, S. Saarakkala, R.K. Korhonen, L. Rieppo, Micro-computed tomography-based collagen orientation and anisotropy analysis of rabbit articular cartilage, Ann. Biomed. Eng. 51 (2023) 1769–1780, https://doi.org/10.1007/s10439-023-03183-4.
[106] A. Silveira, I. Greving, E. Longo, M. Scheel, T. Weitkamp, C. Fleck, R. Shahar, P. Zaslansky, Deep learning to overcome Zernike phase-contrast nanoCT artifacts for automated micro-nano porosity segmentation in bone, J. Synchrotron. Radiat. 31 (2024) 136–149, https://doi.org/10.1107/S1600577523009852.
[107] D.M. Grass, G. Malek, H.M. Taïeb, E. Ittah, H. Richard, N. Reznikov, S. Laverty, Characterization and quantification of in-vitro equine bone resorption in 3D using μct and deep learning-aided feature segmentation, Bone 185 (2024) 117131, https://doi.org/10.1016/j.bone.2024.117131.